Bulk-rock and mineral-scale geochemical evidence of open-system magmatic processes in the felsic rocks of the northern part of the Ditrău Alkaline Massif (Eastern Carpathians, Romania)

LUCA KIRI[1,✉], MÁTÉ SZEMERÉDI[1,2], SASKIA ERDMANN[3],
ANIKÓ BATKI[1,2] and ELEMÉR PÁL-MOLNÁR[1,2]

[1]'Vulcano' Petrology and Geochemistry Research Group, Department of Mineralogy, Geochemistry and Petrology, University of Szeged, 2 Egyetem utca, 6722 Szeged, Hungary;
✉kiri.luca@gmail.com, szemeredi.mate@gmail.com, batki@geo.u-szeged.hu, palm@geo.u-szeged.hu
[2]HUN-REN-ELTE Volcanology Research Group, 1/C Pázmány Péter sétány, 1117 Budapest, Hungary
[3]Université d'Orléans, CNRS/INSU-ISTO-BRGM, UMR 7327, 1A Rue de la Ferollerie Campus Géosciences, 45100 Orléans, France;
saskia.erdmann@cnrs-orleans.fr

Abstract: The felsic suite in the northern part of the Ditrău Alkaline Massif has previously been considered as a homogeneous, uniform unit of the igneous complex. However, these felsic rocks exhibit remarkable diversity on the microscale. Petrographic observations were complemented by bulk-rock and mineral-scale geochemical data to further support this hypothesis. Whole-rock composition of the studied rocks validates the presence of two, compositionally-different felsic cumulate piles in the massif (characterised by Eu/Eu*=2.5–6.7, ΣREE=125–206 ppm and Eu/Eu*=1.0–1.1, ΣREE=358–688 ppm, respectively). Mineral chemical data (amphibole, clinopyroxene, and plagioclase) were acquired from crystals of different textural positions (clot-forming and isolated) to understand which of the ferromagnesian minerals and plagioclase have the highest potential for recognising distinct magmatic environments and open-system magmatic processes. The composition of clinopyroxenes (diopside with mg#=0.77 and 0.85, respectively) overlaps with the formerly published data. Moreover, a new, cumulus-phase occurrence of the clinopyroxenes with a convex REE pattern has been identified. Abrupt changes of Ba, Sr, TiO$_2$ and ΣREE concentrations in different domains of the zoned amphibole crystals and variations in the MgO, FeO, TiO$_2$, Sr, Ba, La, Ce, and anorthite content in plagioclase crystals, together with the bulk-rock data point to the hybrid nature of the majority of the investigated rocks. Our recent geochemical data support the previous, predominantly petrography-based assumptions that the felsic suite in the northern area of the massif was formed in a dynamic, open-system magmatic environment, wherein crystal settling, magma mixing, crystal/mush transfer, and recycling as well as country rock assimilation, prevailed.

Keywords: Eastern Carpathians, Ditrău Alkaline Massif, felsic cumulate, hybridisation, magma mixing, mineral chemistry

Introduction

Many plutonic rocks are partial cumulates or were formed by open-system, igneous processes. Therefore, it is difficult, if not impossible, to evaluate the evolution of their parental melt from bulk-rock data (Deering & Bachmann 2010; Coint et al. 2013). In contrast, mineral textures and composition – particularly mineral-scale trace element compositions and compositional variation – record igneous processes more accurately (e.g., crystal transfer and recycling, fractional crystallisation, magma mingling and mixing), including the associated heterogeneity of the magmatic system (Słaby et al. 2007, 2011; Coint et al. 2013; Barnes et al. 2016). During magma mixing or crystal recycling, the crystallising minerals come into contact with magmas of distinct physicochemical properties (Słaby et al. 2007), which then create a subtle-to-drastic, crystal-scale variation (Barnes et al. 2016): complex growth and/or

disequilibrium textures and zones with different geochemical compositions are formed within individual crystals (Hibbard 1981; Baxter & Feely 2002; Perugini et al. 2006; Kahl et al. 2011, 2015, 2017; Gros et al. 2020). Shifts in the major and trace element concentrations across a single crystal can be used as a proxy to track the changes in the melt composition or other intensive parameters (e.g., pressure and temperature; Słaby et al. 2007, 2011; Coint et al. 2013). In mafic-to-moderately evolved metaluminous-to-peralkaline granitic magmas, clinopyroxene and/or amphibole are common liquidus or near-liquidus phases (e.g., Scaillet et al. 2016; Huang et al. 2019), which incorporate a large spectrum of trace elements that range from large ion lithophile over rare earth to high field strength elements (LILEs, REEs, HFSEs, respectively; e.g., Naney 1983; Marks et al. 2004). In combination, both minerals may record near-liquidus to near-solidus evolution of magmas, which thus reflect their relatively large stability

fields and refractory nature (slow diffusivities for key compositional constituents; e.g., Costa 2021). Therefore, amphibole and clinopyroxene chemistry can be applied to unravel the igneous evolution and, ideally, the composition of the parental melt (e.g., Piwinskii 1968; Naney 1983; Schmidt 1992; Marks et al. 2004; Ubide et al. 2014a). Similarly, plagioclase crystallises over an extensive spectrum of magma compositions, as well as over a large range of temperature (e.g., Wiebe 1968; Anderson 1984; Blundy & Wood 1991; Putirka 2005). Although the concentration of trace elements and the type of trace elements that are incorporated by plagioclase are significantly lower than in clinopyroxene and amphibole crystals, some of the elements (e.g., Sr and Ba) are particularly useful for deciphering the igneous processes (Blundy & Shimizu 1991; Ginibre et al. 2002; Grogan & Reavy 2002). Intracrystalline diffusion and thus the equilibration of major elements and several trace elements (e.g., Sr, Ba, REEs) is slow, and their concentration commonly records compositional and other changes of intensive parameters of the host magmas precisely (e.g., pressure and temperature; Smith et al. 2009).

The main objective of this research was to discern which of the studied mafic minerals (magmatic and secondary amphibole, as well as clinopyroxene) and plagioclase have the highest potential to distinguish different igneous environments and to reveal open-system magmatic processes. New mineral major and trace element data along with whole-rock compositions are presented to further understand the petrogenesis of the felsic suite in the northern part of the Ditrău Alkaline Massif (DAM), thereby complementing previous field and petrographic observations.

Geologic setting

The DAM is situated in the Eastern Carpathians (Romania) and belongs to the Dacia Mega-Unit (Fig. 1A, B). It forms the south-western and southern areas of the Giurgeu Mts. and extends over an area of ca. 225 km^2. The massif consists of different rock types in a spectrum from ultramafic cumulates to granitoid rocks (Streckeisen & Hunziker 1974; Jakab 1998; Kräutner & Bindea 1998; Morogan et al. 2000; Pál-Molnár 2000; Batki et al. 2014; Pál-Molnár et al. 2015a, b; Fig. 1C).

In the Middle-Late Triassic, an igneous event occurred near the southern margin of the East European craton in an intraplate, rift-related, extensional tectonic regime. Recent geochronological data suggest a brief magmatic period (Ladinian–Norian) for the formation of the DAM (e.g., Pál-Molnár et al. 2021; Klötzli et al. 2022). The Variscan metamorphic rocks of the Eastern Carpathians had been penetrated by the alkaline magmas of the DAM and were collectively subjected to consecutive nappe-forming Alpine tectonic processes (Fig. 1B). An eastward-verging nappe system was established as a result of the Cretaceous (Austrian) tectogenesis. It is referred to as either Eastern Getides (Balintoni 1997) or Median Dacides (Săndulescu 1984). The Infrabucovinian,

Subbucovinian, and Bucovinian Nappes (with pre-Alpine metamorphic rocks and Permo–Mesozoic cover series) make up the Median Dacides (Săndulescu 1984). Pre-Alpine, petrographically-analogous tectonic units occur in the Subbucovinian and Bucovinian Nappes. The DAM is structurally associated with the Bucovinian Nappe (Fig. 1B) and juxtaposed with four of its pre-Alpine metamorphic terranes (Bretila, Tulgheş, Negrişoara, and Rebra Lithogroups; Balintoni et al. 2014). A tectonic discontinuity separates the DAM from the Subbucovinian Nappe because the massif was uprooted during the Alpine tectonic events and was thus split by the Bucovinian shear zone (Kräutner & Bindea 1995).

In the northern part of the DAM, from west to east, the massif comprises a sequence of ultramafic and mafic cumulates that grade into gabbro, diorite (s.l.), monzonite, syenite, quartz syenite, and granite (Fig. 1C). Nepheline syenite forms an extensive area in the central and eastern parts of the massif, associated with minor syenite and granite (Pál-Molnár 2000; Pál-Molnár et al. 2015a, b). The spatially-related (ultra)mafic rocks [hornblendite, gabbro, and diorite (s.l.)] in the northwestern part of the massif form a lithostratigraphic unit of a complex structure [referred to as the Tarniţa Complex (Pál-Molnár 2000)]. Apart from the mingling structures of different diorite types (s.l.) (Fig. 2A) near the confluence of the Pietrăriei de Sus and Jolotca Creeks (Heincz et al. 2018), no other intrusive contacts were found in this region. Mingling structures of diorite (s.l.) and nepheline syenite can be studied in the outcrops along the Ditrău–Hagota road (central part of the DAM), evidenced by mafic enclaves (Fig. 2B) and large mafic (Fig. 2C), as well as felsic cumulate fragments (Fig. 2D). The rocks of the massif are crosscut by lamprophyre, (nepheline) syenite, ijolite, and tinguaite dykes (Pál-Molnár 2000; Batki et al. 2014; Pál-Molnár et al. 2015a, b; Fig. 2A, E). Wall rock xenoliths are present along the contact between syenite, monzogranite, and the metamorphic country rocks (e.g., Kräutner & Bindea 1995; Kiri et al. 2022; Fig. 3C). Based on amphibole thermobarometry, the (ultra)mafic cumulates are lower-crust derived (Pál-Molnár et al. 2015a); whereas granite was emplaced at middle to upper crustal depths (Pál-Molnár et al. 2015b). P–T conditions for the formation of other lithologies are not available (e.g., monzonite and syenite).

Previous studies have interpreted the felsic suite of the northern part of the DAM as a homogeneous, uniform unit of the massif (e.g., Jakab 1998; Kovács & Pál-Molnár 2005). Nevertheless, recent investigations have suggested that the felsic rocks were formed in an open-system magmatic environment (e.g., Batki et al. 2018; Heincz et al. 2018; Ódri et al. 2020; Kiri et al. 2022). A detailed petrographic study of the felsic suite in the northern area of the DAM revealed microtextural features (e.g., mafic clots, plagioclase crystals in synneusis relation, adjacent plagioclase feldspars with disparate zoning patterns, country rock xenoliths) indicative of dynamic magmatic conditions (e.g., crystal transfer and recycling, cumulate formation, magma mixing and mingling, as well as wall rock assimilation; Kiri et al. 2022). However,
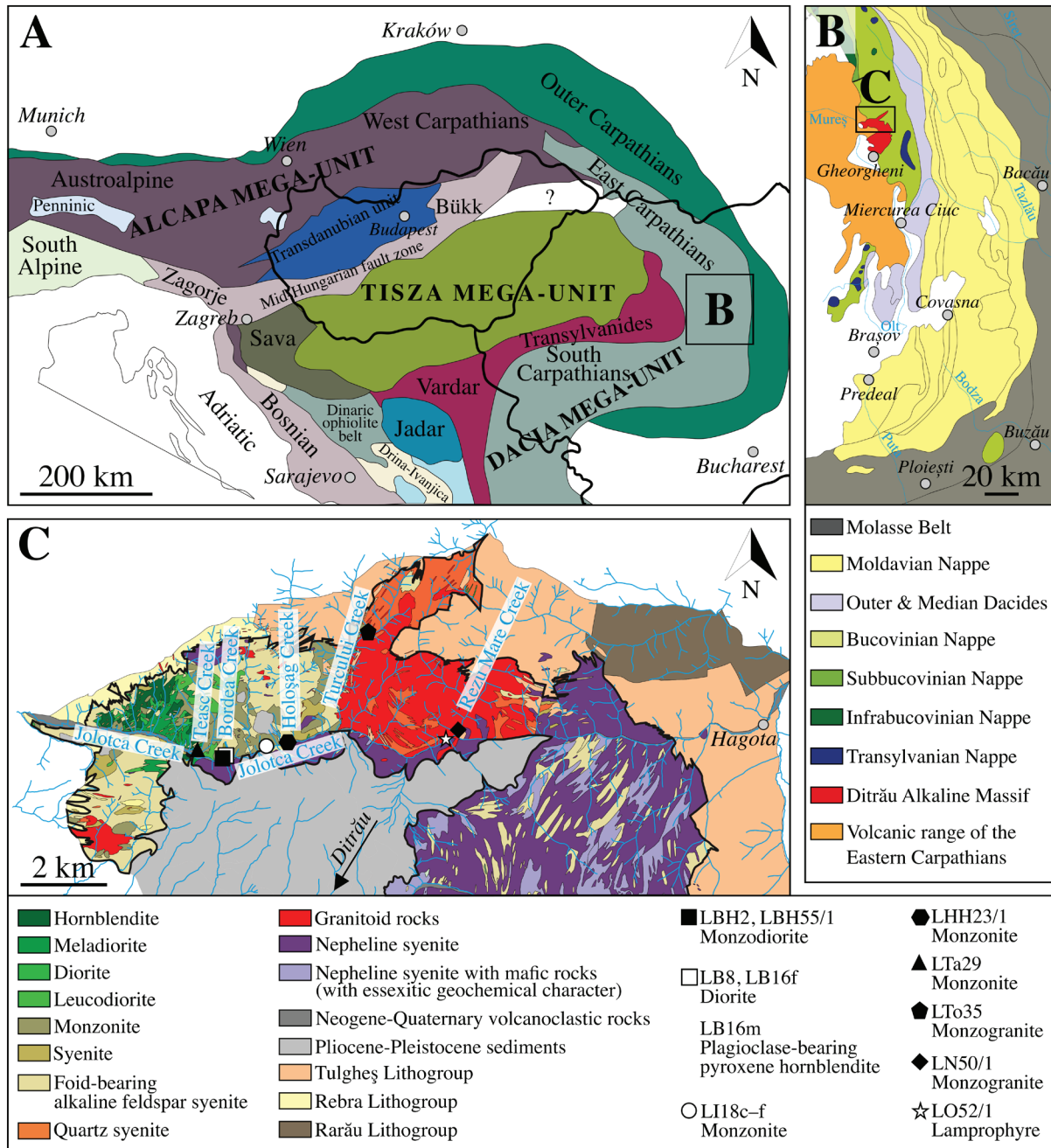
Fig. 1. A — Position of the Ditrău Alkaline Massif in the Alpine-Carpathian-Dinaric realm (modified after Haas et al. 2010). **B** — Location of the massif in the Alpine tectonic units of the Eastern Carpathians (modified after Săndulescu et al. 1981). **C** — Sampling sites of various rock types (details in legend) in the schematic geological map of the northern part of the massif (modified after Pál-Molnár et al. 2015a). The figure is modified after Kiri et al. (2022).

sparse geochemical data for the felsic rocks (e.g., Batki et al. 2018; Ódri et al. 2020) and the lacking mineral-scale compositional data needed to be supplemented to validate this concept.

Batki et al. (2018) distinguished two parental magmas based on the composition of clinopyroxene populations from olivine-rich and pyroxene-rich cumulates, diorite, syenite, nepheline syenite, camptonite, and tinguaite dykes along with ijolite enclaves: Magma1 (M1) of basanitic composition,

parental to (ultra)mafic cumulates and rocks of the Tarnița Complex along with Magma2 (M2) that evolved to a phonolitic composition. Interaction between the two magmas was evidenced by the presence of green clinopyroxene antecrysts in diorite, syenite, and tinguaite; however, the evolution of the felsic suite [e.g., the open-system processes involved in the formation of syenite (crustal assimilation, magma mixing) and its genetic relation to the other rock types of the massif] remained partly unresolved (Batki et al. 2018).
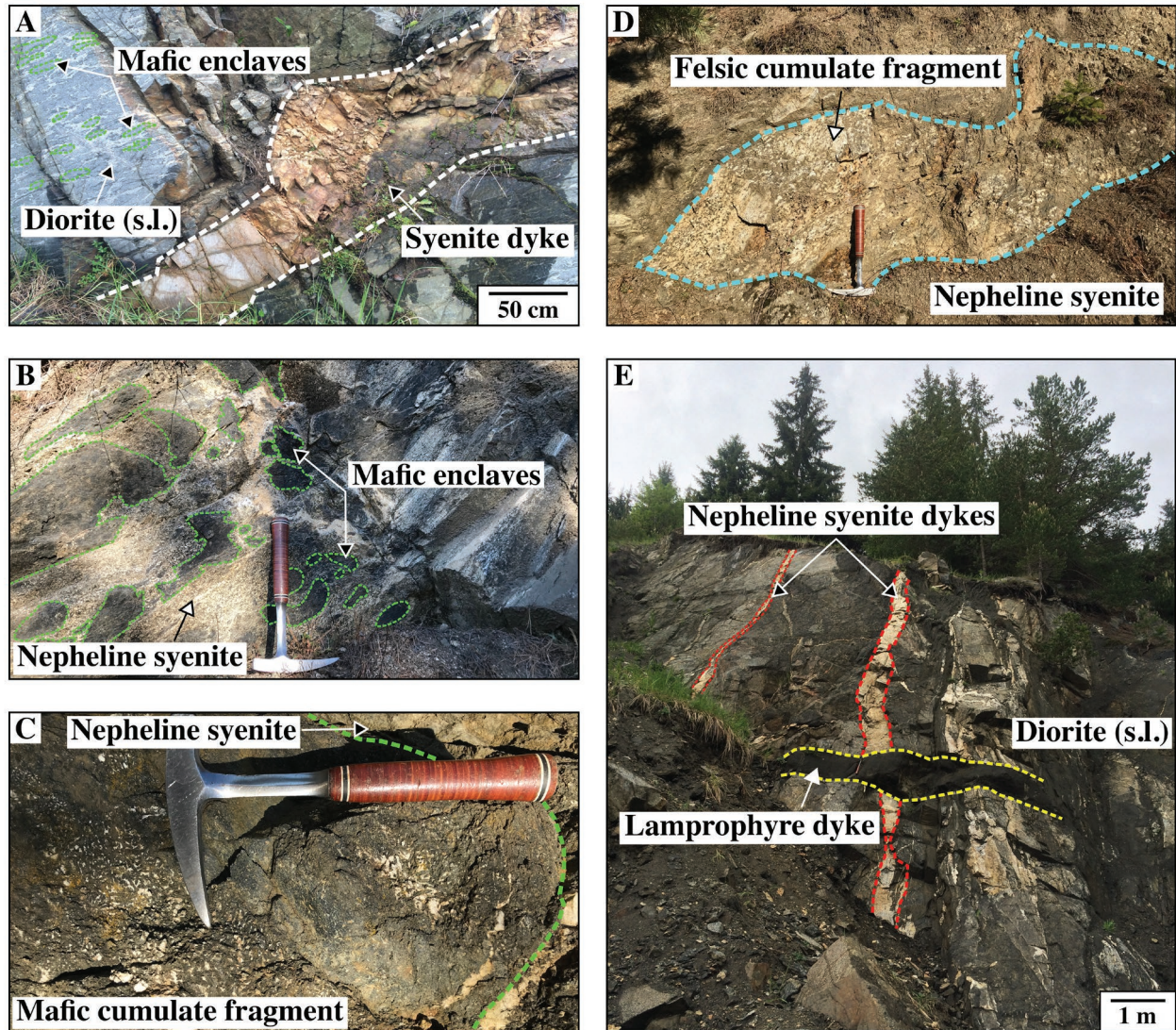
Fig. 2. Field evidence for interactions between different magma batches. **A** — Syenite dyke crosscutting the host rock and the mafic enclaves in the Tarnița Complex. **B** — Mafic enclaves. **C** — Mafic cumulate fragment. **D** — Felsic cumulate fragment. **E** — Nepheline syenite and lamprophyre dykes in outcrops along the Ditrău–Hagota road.

Materials and analytical methods

Samples

A detailed description of the sampling area along with the macroscopic and microscopic characteristics of the collected rocks can be found in Kiri et al. (2022), since only a brief summary is presented here (Table 1; Supplementary Table S1). In line with the classification schemes used in previous studies (e.g., Pál-Molnár et al. 2015a; Heincz et al. 2018; Kiri et al. 2022), the nomenclature used in this paper is based on the modal composition of the studied rocks to ensure comparability. Two groups of felsic rocks were identified in accordance with field occurrences and microtextures: Group 1 – felsic rocks (diorite) with a minor mafic mineral content, spatially-associated with mafic cumulates (plagioclase-bearing pyro-xene hornblendite) and Group 2 – felsic rocks (monzodiorite, monzogranite, monzonite, nepheline-bearing syenite, quartz monzonite, quartz syenite, syenite, syenogranite), which comprise mafic minerals and aggregates and are not spatially associated with mafic cumulates (Kiri et al. 2022). Plagioclase (85–87 vol%) predominates in the rocks of the first group; whereas, biotite (4–9 vol%), alkaline feldspar (2–8 vol%), and titanite (max. 1 vol%) occur in minor amounts (Fig. 3A). The structural and textural characteristics of the rock-forming minerals [e.g., impinging plagioclase feldspars with separate cores, clusters of multiple plagioclase crystals in parallel orientation ("chain structure"; Vernon & Collins 2011; Fig. 4A,B)] imply that these rocks were formed by crystal accumulation. In the rocks of Group 2, the felsic rock-forming minerals are represented by plagioclase (8–71 vol%), alkaline feldspar (22–78 vol%), and quartz (0–46 vol%; Fig. 3B–D).

Discrete, primary mafic minerals are rare (amphibole: max. 6 vol%; biotite: max. 9 vol%); however, various clusters (max. 18 vol%) which comprise either one or multiple mafic mineral types are prevalent (Fig. 4E–H; Supplementary Table S1). Titanite is the most common accessory mineral (max. 2 vol%). Some of the rocks in the second group also exhibit textural traits that are analogous to that of Group 1; thus indicating crystal accumulation (Fig. 4C, D).
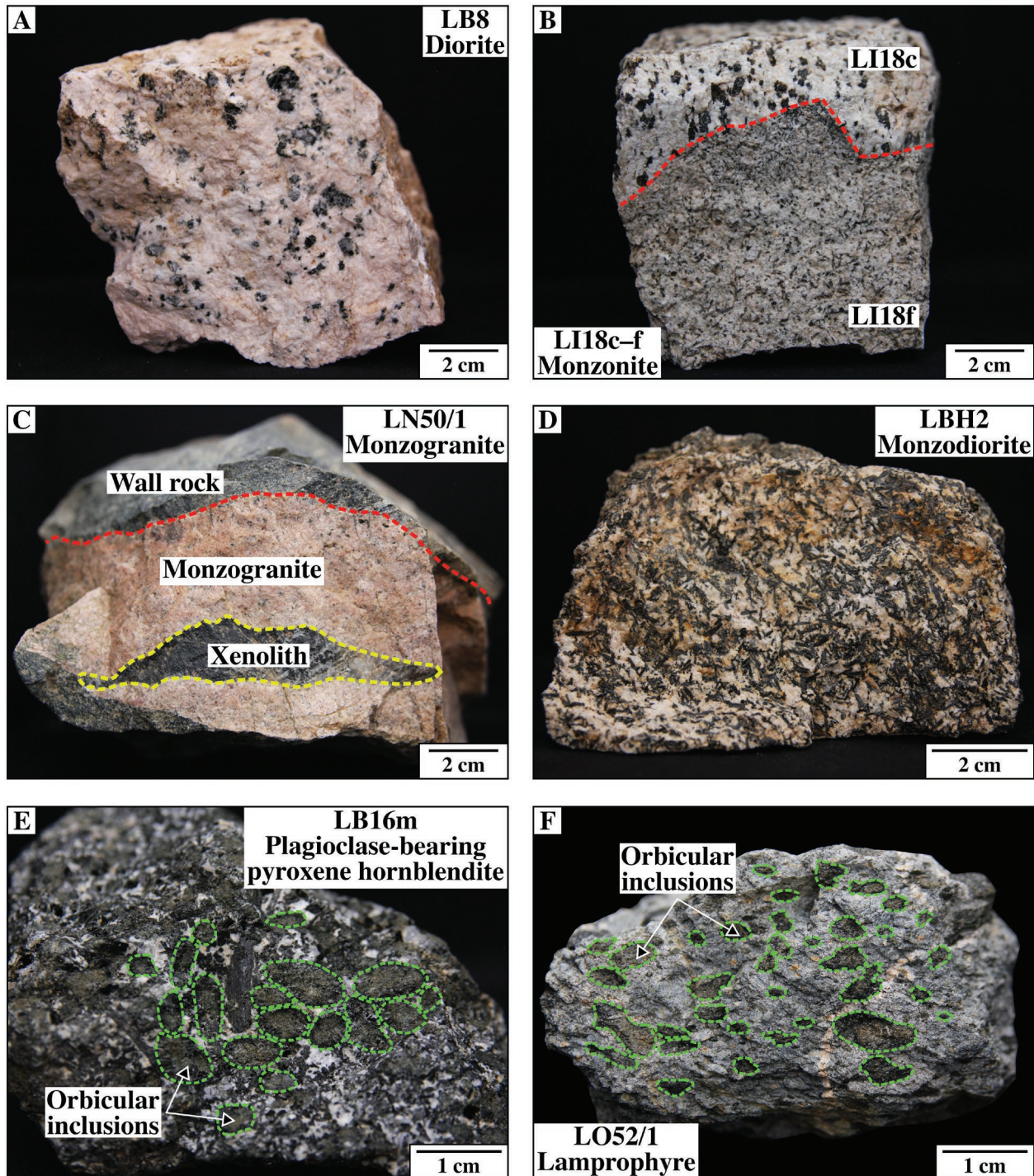
Fig. 3. Macroscopic textural characteristics of the studied rocks (modified after Kiri et al. 2022). **A** — Disseminated biotite flakes. **B** — Contact (highlighted by a red dashed line) between monzonite and monzonite dyke. **C** — Hornfels xenolith in monzogranite. The margin of the xenolith is marked in yellow, while the contact of monzogranite and the metamorphic wall rock is highlighted by a red dashed line. **D** — Isolated and clot-forming amphibole crystals. **E, F** — Orbicular inclusions with a clinopyroxene core rimmed by amphibole and biotite of the host (marked by green dashed lines) in plagioclase-bearing pyroxene hornblendite and lamprophyre, respectively.

Table 1: Nomenclature, sampling locations, main petrographic features and whole-rock major and trace element compositions of the studied rocks from the Ditrău Alkaline Massif (Romania). Rock type abbreviations: D – diorite, Do – diorite with oriented texture, FM – foid-bearing monzonite, FMD – foid-bearing monzodiorite, FS – foid-bearing syenite, G – granite, L – lamprophyre, M – monzonite, Mo – monzonite with oriented texture, MDo – monzodiorite with oriented texture, MG – monzogranite, PIPxH – plagioclase-bearing pyroxene hornblendite, QM – quartz monzonite, S – syenite.

| Sample	LBH2	LB8	LB16f (felsic part)	LB16m (mafic part)	LI18f (fine-grained)	LI18c (coarse-grained)	LHH23/1	LTa29	LTo35	LN50/1	LO52/1	LBH55/1
Rock type (modal composition and texture)	MDo	D	Do	PIPxH	Mo	M	M	M	MG	MG	L	MDo
Rock type (total alkali vs. SiO$_2$)	M	S	S	–	M	S	M	M	QM	G	–	M
Rock type (calculated cation norms)	FMD	FMD	FMD	–	FM	FM	FS	FM	QM	MG	–	FM
Locality and GPS coordinates	Hillside west of the Bordea creek 46.86200, 25.51558	Bordea creek 46.86246, 25.51698	Bordea creek 46.86235, 25.51704	Bordea creek 46.86235, 25.51705	Behind the school in Jolotca 46.86448, 25.52762	Behind the school in Jolotca 46.86448, 25.52762	Hillside west of the Holosag creek 46.86579, 25.53452	Teasc creek 46.86344, 25.50844	Turcului creek 46.8887, 25.55766	Rezu Mare creek 46.86842, 25.58544	Jolotca creek 46.86653, 25.58137	Hillside west of the Bordea creek 46.86196, 25.51556
Rock group	2	1	1	–	2	2	2	2	2	2	–	2
Mineral assemblage (primary) and modal composition (vol %)	Pl (62) Afs (31) Amp (3) Bt (2) Ttn (1) Opq (<1)	Pl (87) Afs (2) Bt (9) Ttn (1)	Pl (85) Afs (8) Bt (4)	Pl (61) Cpx (4) Amp (5) Bt (30)	Pl (43) Afs (53) Amp (1) Bt (2) Ttn (1)	Pl (50) Afs (43) Amp (6) Bt (<1) Ttn (<1)	Pl (56) Afs (38) Bt (6)	Pl (42) Afs (51) Amp (2) Bt (1) Ttn (2)	Pl (36) Afs (35) Qtz (24) Amp (3) Bt (2)	Pl (20) Afs (28) Qtz (46) Bt (6)	Pl (60) Cpx (2) Amp (21) Bt (15) Ttn (2)	Pl (71) Afs (22) Bt (7)
Major elements (wt %)												
SiO$_2$	53.43	62.60	60.74	n.d.	57.71	58.74	55.65	55.69	63.72	75.68	n.d.	57.19
TiO$_2$	2.06	0.48	0.66	n.d.	0.83	1.02	1.13	1.69	0.74	0.13	n.d.	0.77
Al$_2$O$_3$	18.02	20.52	21.65	n.d.	20.08	19.27	18.94	18.55	17.01	12.84	n.d.	21.13
Fe$_2$O$_3$	8.50	2.02	2.13	n.d.	5.01	4.47	8.22	6.64	4.18	1.77	n.d.	4.90
MnO	0.22	0.03	0.03	n.d.	0.16	0.14	0.18	0.12	0.09	0.03	n.d.	0.08
MgO	1.74	0.57	0.53	n.d.	0.61	0.78	2.62	1.48	0.92	0.15	n.d.	0.96
CaO	5.77	2.19	3.09	n.d.	3.44	3.31	1.14	4.56	2.06	0.54	n.d.	2.84
Na$_2$O	6.14	9.54	8.53	n.d.	6.31	6.00	6.44	5.44	4.72	4.11	n.d.	6.77
K$_2$O	2.46	0.91	1.49	n.d.	4.11	4.99	3.55	4.00	4.84	4.24	n.d.	3.64
P$_2$O$_5$	0.35	0.05	0.07	n.d.	0.12	0.19	<0.01	0.30	0.22	0.02	n.d.	0.28
Cr$_2$O$_3$	0.00	0.00	0.00	n.d.	<0.002	<0.002	0.02	<0.002	<0.002	0.00	n.d.	<0.002
LOI	0.80	0.80	0.70	n.d.	0.80	0.50	1.70	0.80	1.20	0.40	n.d.	1.00
Total	99.57	99.83	99.74	n.d.	99.43	99.64	99.71	99.59	99.79	99.92	n.d.	99.76
mg#	0.29	0.36	0.33	n.d.	0.19	0.26	0.39	0.31	0.30	0.14	n.d.	0.28
Normative minerals (wt %)												
Ne	2.04	1.58	2.45	n.d.	3.05	2.52	0.37	0.41	0.00	0.00	n.d.	3.68
Ol	1.38	0.99	0.93	n.d.	0.74	0.71	4.57	1.94	0.00	0.00	n.d.	1.68
D.I.	79.50	95.25	94.98	n.d.	90.22	89.84	81.46	84.76	90.2	96.62	n.d.	89.56

Table 1 (continued)

Sample	LBH2	LB8	LB16f (felsic part)	LB16m (mafic part)	LI18f (fine-grained)	LI18c (coarse-grained)	LHH23/1	LTa29	LTo35	LN50/1	LO52/1	LBH55/1
Trace elements (ppm)												
Be	6.00	2.00	2.00	n.d.	8.00	2.00	2.00	2.00	6.00	12.00	n.d.	2.00
Sn	3.00	<1	<1	n.d.	3.00	2.00	<1	2.00	3.00	2.00	n.d.	<1
W	0.70	<0.5	<0.5	n.d.	0.60	<0.5	0.50	<0.5	1.60	2.00	n.d.	1.50
Sc	3.00	<1	<1	n.d.	1.00	2.00	1.00	3.00	3.00	<1	n.d.	3.00
V	92.00	21.00	22.00	n.d.	32.00	36.00	46.00	87.00	33.00	<8	n.d.	98.00
Co	10.20	3.60	5.90	n.d.	3.50	4.00	9.20	10.30	5.00	1.00	n.d.	7.70
Ni	<20	<20	<20	n.d.	<20	<20	40.00	<20	<20	<20	n.d.	<20
Ga	22.50	16.10	19.20	n.d.	25.30	21.00	22.60	18.10	22.30	22.00	n.d.	21.10
Rb	45.90	20.20	30.30	n.d.	80.60	99.00	103.00	46.90	156.60	143.00	n.d.	102.60
Sr	1404.00	1238.90	1676.30	n.d.	2455.10	1587.70	412.50	2040.10	557.50	44.80	n.d.	1171.60
Y	42.20	7.30	11.10	n.d.	32.40	29.30	3.80	32.50	20.60	23.70	n.d.	6.40
Zr	523.40	64.70	135.30	n.d.	913.60	459.30	1009.40	248.70	483.00	126.90	n.d.	179.30
Nb	245.80	36.60	56.80	n.d.	206.00	138.30	36.00	186.00	87.90	114.40	n.d.	39.80
Cs	0.70	<0.1	0.30	n.d.	1.40	0.90	1.00	0.30	2.80	1.90	n.d.	0.80
Ba	1009.00	856.00	770.00	n.d.	1978.00	1943.00	636.00	2561.00	912.00	86.00	n.d.	1494.00
La	174.50	25.60	38.70	n.d.	233.50	104.60	60.30	125.70	41.00	16.40	n.d.	73.60
Ce	311.00	43.20	67.50	n.d.	328.90	184.30	48.20	228.50	90.70	33.40	n.d.	89.80
Pr	29.60	4.35	6.79	n.d.	27.76	18.29	2.67	22.79	7.78	4.05	n.d.	6.82
Nd	96.40	14.90	22.70	n.d.	83.00	61.20	6.10	75.90	27.70	15.10	n.d.	19.90
Sm	13.77	2.38	3.60	n.d.	10.90	9.19	0.44	10.83	5.16	3.75	n.d.	2.36
Eu	4.07	0.90	1.20	n.d.	3.28	2.70	0.96	3.25	1.52	0.67	n.d.	1.75
Gd	10.49	1.89	2.94	n.d.	7.86	7.32	0.43	8.35	4.49	4.01	n.d.	1.89
Tb	1.54	0.27	0.43	n.d.	1.12	1.08	0.06	1.21	0.68	0.73	n.d.	0.20
Dy	8.12	1.54	2.25	n.d.	6.18	5.59	0.50	6.36	4.01	4.81	n.d.	1.18
Ho	1.47	0.24	0.40	n.d.	1.13	1.10	0.13	1.17	0.74	0.93	n.d.	0.22
Er	4.13	0.67	1.16	n.d.	3.43	3.22	0.47	3.49	2.24	3.08	n.d.	0.59
Tm	0.56	0.09	0.15	n.d.	0.46	0.40	0.08	0.41	0.32	0.46	n.d.	0.09
Yb	3.39	0.53	0.82	n.d.	2.99	2.65	0.70	2.63	2.27	2.94	n.d.	0.66
Lu	0.45	0.06	0.10	n.d.	0.48	0.39	0.14	0.30	0.33	0.45	n.d.	0.10
Hf	12.90	1.50	2.90	n.d.	16.50	9.30	19.10	6.70	10.60	5.50	n.d.	3.40
Ta	15.50	3.10	4.70	n.d.	11.00	7.80	0.70	12.50	5.80	13.20	n.d.	1.20
Th	16.10	3.40	10.90	n.d.	40.90	11.00	1.70	9.30	16.50	61.00	n.d.	8.20
U	3.80	0.80	3.90	n.d.	6.00	2.40	0.90	1.50	3.20	9.80	n.d.	1.50
ΣREE	1493.09	209.03	360.81	n.d.	1888.00	1040.67	1189.56	970.79	794.14	376.42	n.d.	429.10
$(La/Sm)_N$	7.91	6.72	6.71	n.d.	13.38	7.11	85.58	7.25	4.96	2.73	n.d.	19.48
$(Gd/Yb)_N$	2.50	2.89	2.90	n.d.	2.13	2.23	0.50	2.57	1.60	1.10	n.d.	2.32
Eu/Eu^*	1.03	1.29	1.12	n.d.	1.08	1.00	6.73	1.04	0.96	0.53	n.d.	2.53

Rock type abbreviations: D – diorite, Do – diorite with oriented texture, FM – foid-bearing monzonite, FMD – foid-bearing monzodiorite, FS – foid-bearing syenite, G – granite, L – lamprophyre, M – monzonite, Mo – monzonite with oriented texture, MDo – monzodiorite with oriented texture, MG – monzogranite, PIPxH – plagioclase-bearing pyroxene hornblendite, QM – quartz monzonite, S – syenite
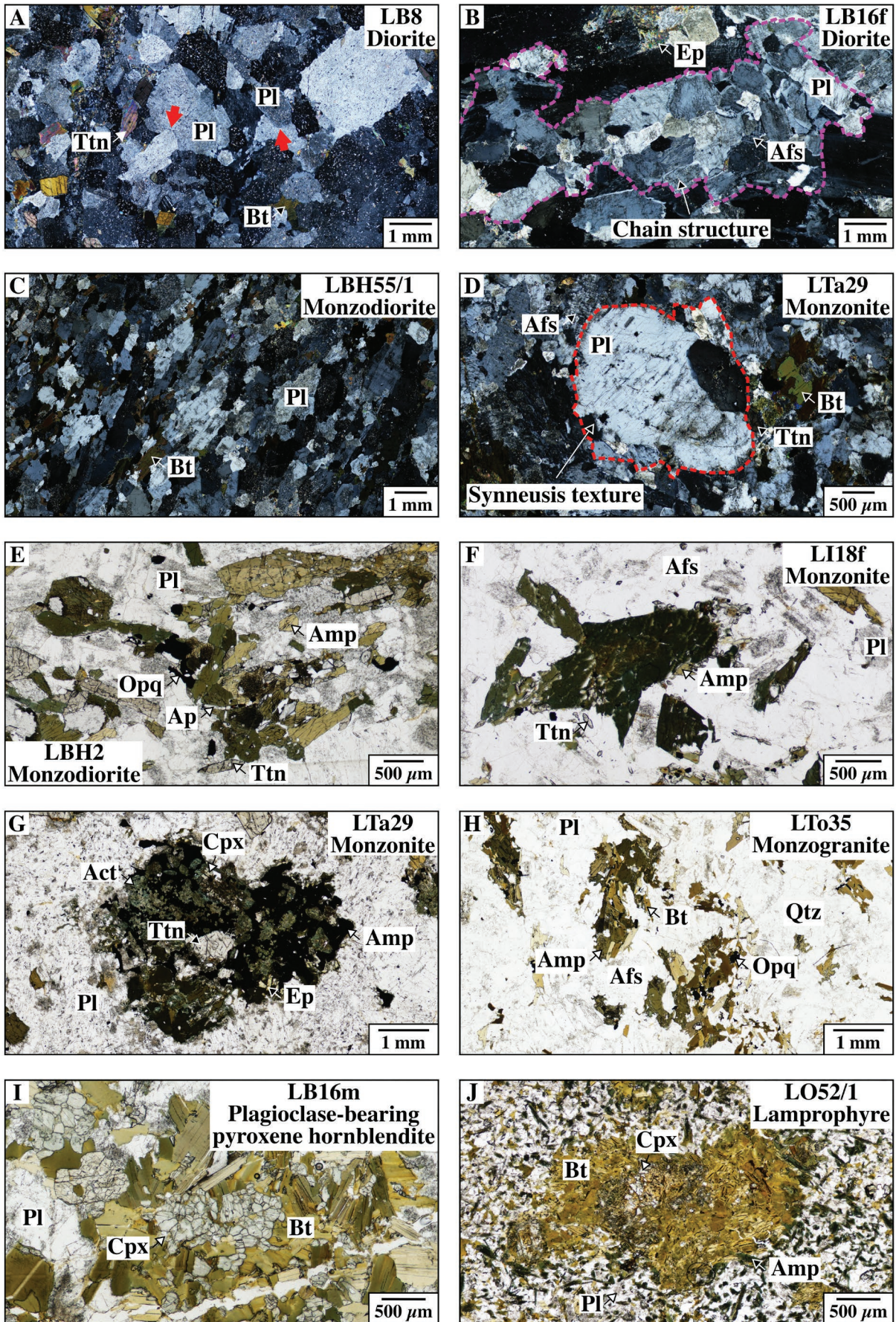
Fig. 4. Characteristic micro-scale textural features of the studied rocks. **A** — Impinging plagioclase crystals (marked by the red arrows), +N (crossed polars); **B** — Chain structure of plagioclase crystals in parallel orientation (the aggregate is highlighted by a pink dashed line), +N; **C** — Parallelly-aligned biotite and plagioclase, +N; **D** — Plagioclase megacryst with smaller-sized grains in synneusis relation (the cluster is highlighted by a red dashed line), +N; **E, F** — Amphibole aggregates, 1N (plane polarised light); **G** — Polymineralic *AmpCpxTtnOpqBt* aggregate, 1N; **H** — *AmpBt* clusters, 1N; **I, J** — Orbicular inclusions with a clinopyroxene core rimmed by amphibole and biotite crystals, 1N. Clot type abbreviations: *AmpBt* – amphibole+biotite cluster, *AmpCpxTtnOpqBt* – amphibole+clinopyroxene+titanite+opaque minerals ±biotite aggregate. The names of the minerals were abbreviated following the classification scheme of Whitney & Evans (2010).

Exposures are rare due to recent recultivation and dense vegetation; hence, samples were collected from *in situ* outcrops from hillsides and the valleys of creeks.

The rocks to be analysed for bulk rock and/or mineral compositions (Table 1) were selected according to the following criteria: (a) to include the most important felsic rock types (diorite, monzodiorite, monzogranite, monzonite), as well as ferromagnesian minerals (amphibole and clinopyroxene) from mafic rocks (plagioclase-bearing pyroxene hornblendite and lamprophyre) for comparison, which are all typical of the northern area of the massif; (b) to represent all textural types; and (c) to include all textural-mineralogical mafic and felsic (feldspar-rich) crystal-clot varieties.

Bulk-rock major and trace element analyses

The representative felsic rock samples were powdered and analysed at the Bureau Veritas Mineral Laboratories (ACMELabs, Vancouver, Canada). The whole-rock composition of plagioclase-bearing pyroxene hornblendite and lamprophyre was not determined (they were only characterised petrographically) as comprehensive data for similar rock types are readily available in previous research (e.g., Batki et al. 2014; Pál-Molnár et al. 2015a). Major element concentrations were determined by ICP-ES (detection limit: 0.01–0.04 wt%), whereas trace element compositions were measured using ICP-MS. The samples were split and a 0.2 g sample was used for $LiBO_2/Li_2B_4O_7$ fusion decomposition for ICP-ES and a 0.2 g sample for ICP-MS. The STD SO-19 and QUARTZ_KRA (pure quartz) internal geological reference materials were applied to control the analytical accuracy (better than ±1.5 %). Duplicate samples were used in each analytical set to verify the precision (better than 0.5 % for the repeated measurements). After ignition at 1000 °C for 4 hours, the weight difference was applied to calculate the loss on ignition (LOI).

In situ mineral major and trace element analyses

Mineral major and trace element concentrations were determined on crystals from polished thin sections (30 μm thickness). Minerals selected for analysis were those that are common in almost all rock types of the northern part of the massif (amphibole, clinopyroxene, and plagioclase) – including amphibole and clinopyroxene crystals of plagioclase-bearing pyroxene hornblendite (LB16m) and lamprophyre (LO52/1; Figs. 3E, F and 4I, J) that were measured for comparison. Mafic and felsic minerals in different textural positions (occurring as isolated crystals in the "groundmass", as well as

clot-forming minerals) were selected to track any compositional differences. It must be elucidated that the term "groundmass" used in this paper refers to the main mass of the host rock: the holocrystalline, phaneritic, and generally felsic mineral-rich domain that encircles mafic crystal clusters.

The zonation and compositional variation of the minerals were investigated optically (by transmitted light and back-scattered electron microscopy) and characterised quantitatively (by SEM BSE, EMPA, and LA-ICP-MS). An AMRAY 1830 SEM coupled with an EDAX PV 9800 EDS detector at the Department of Petrology and Geochemistry, Eötvös Loránd University, Budapest, Hungary was applied to acquire backscattered electron images (Fig. 5). The BSE images, along with microphotographs, were implemented to reveal compositional zonation and to determine the position of the analytical spots. In the absence of optical and SEM zoning, the analytical points (core, transition, rim) were located based on geometric parameters.

Both major- and minor element concentrations of minerals were determined by electron microprobe in wavelength dispersive mode, carried out at the Institut des Sciences de la Terre d'Orléans – Centre National de la Recherche Scientifique (ISTO-CNRS), Orléans, France, using a Cameca SX Five electron microprobe, operated at an acceleration voltage of 15 kV and a beam current of 10 nA, utilising a focused beam. Elements analysed for all sample phases (10 and 5 second counting times on peaks and background, respectively) were Si, Ti, Al, Mg, Mn, Fe, Ca, Na, and K, which are reported as oxide concentrations with Fe recorded as FeO. Calibration standards were natural and synthetic mineral phases (albite: Si, Na; Al_2O_3: Al; andradite: Ca; Fe_2O_3: Fe; $MnTiO_3$: Mn, Ti; olivine: Mg; orthoclase: K), of which albite, andradite, and olivine were also repeatedly analysed as quality control.

The trace element concentrations (including REE) were determined by LA-ICP-MS employing a RESOlution SE laser ablation system connected to an Agilent 8900 QQQ inductively-coupled plasma mass spectrometer at the Institut des Sciences de la Terre d'Orléans – Centre National de la Recherche Scientifique (ISTO-CNRS), Orléans, France. The same spots were analysed as for the EMPA. Ablation was performed with a round laser beam of different diameters (amphibole: 20 and 30 μm; clinopyroxene: 30 μm; plagioclase: 20, 30, and 50 μm) with a frequency of 10 Hz and a fluence of 4 J cm⁻² on the sample surface. The ablations were performed in a mixed Ar (~0.9 l/min) and He (~400 ml/min) atmosphere. The ICP-MS was operated at 1480 W. For the mafic minerals and plagioclase, 33 and 22 isotope concentrations were measured respectively, each with a dwell time of 10 ms. Three
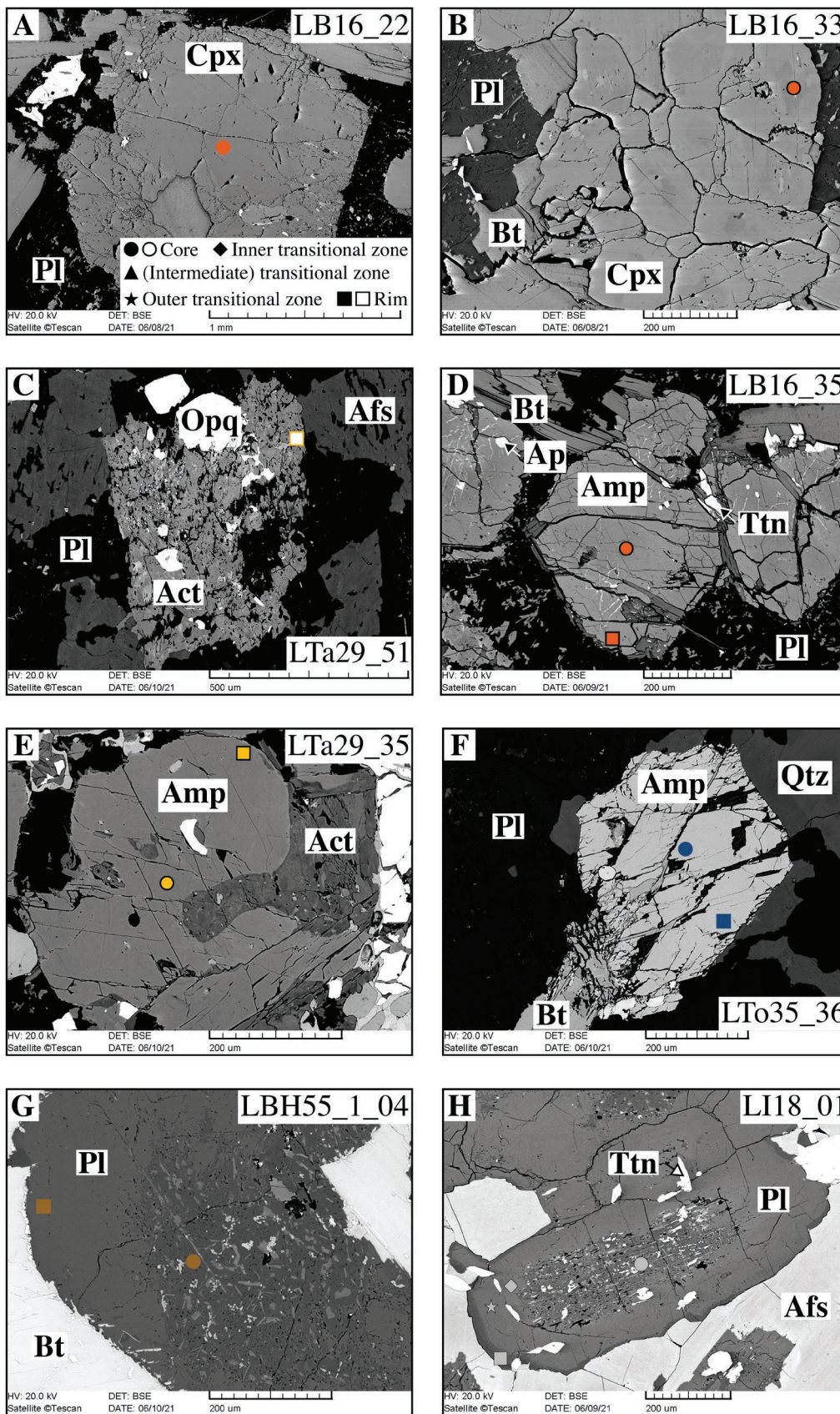
Fig. 5. Representative SEM images of the studied crystals showing where individual analyses were performed. Symbols with black rim mark analyses on clot-forming crystals. **A, B** — Groundmass and orbicular inclusion-derived clinopyroxene, respectively; **C** — Groundmass actinolite; **D, E** — Clot-forming amphibole; **F** — Isolated amphibole; **G** — Reversely-zoned and **H** — complexly-zoned plagioclase crystal.

analyses of the external standard NIST610 were followed by analysis of quality control reference materials NIST612 and BCR-2G, as well as twelve analyses of samples unknown in sequences of 100–200 points. Each analysis comprised a measurement of 20 s gas blank before 30 s laser ablation and a 10 s washout at the end. Ablation signals were individually screened for contaminated analyses. To determine trace element concentrations off-line, Glitter software (van Achterbergh et al. 2001) was used with a linear extrapolation across external standards and SiO_2 determined by electron microprobe as the internal standard. Reference material compositions are the preferred values provided at GeoReM (http://georem.mpch-mainz.gwdg.de/).

Results

Whole-rock major and trace element data

The results of the bulk-rock geochemical analyses can be found in Table 1. Based on their Chemical Index of Alteration (CIA; Nesbitt & Young 1982), the studied samples were subjected to either no weathering or weak weathering. The SiO_2 composition of the analysed rocks covers a wide spectrum (53.4–75.7 wt%; Fig. 6A). Due to their high Na_2O+K_2O content (ranging from 8.4 to 10.9 wt%), the studied rocks are classified as alkaline. In the TAS diagram, the samples are aligned along a single compositional array, which involves the monzonite, syenite, and quartz monzonite compositional fields. The only exception is sample LN50/1 (monzogranite), which deviates from this trend (Fig. 6A).

Although feldspathoids were not identified during our petrographic investigations, the CIPW norm calculations imply that most of the analysed rocks – with the exception of the quartz-bearing samples LTo35 and LN50/1 (monzogranites) – are nepheline-normative (0.4–3.7 vol%) and their composition plots in the "foid-bearing" field in the cation norm classification diagram (Streckeisen & Le Maitre 1979; Fig. 6B; Table 1).

There is a negative correlation between the concentration of SiO_2 and Fe_2O_3, MgO, TiO_2, MnO, and CaO (Fig. 6D–H). In contrast, the data points are scattered for Na_2O and K_2O (Fig. 6I, J).

The differentiation index (D.I., the sum of normative quartz, albite, orthoclase, nepheline, kaliophilite, and leucite; Cross et al. 1902) varies from 79.5 [LBH2 (monzodiorite)] to 96.6 [LN50/1 (monzogranite); Table 1].

Three trends can be identified according to the chondrite-normalised REE patterns of the rocks (Fig. 7A, C, E): (a) LHH23/1 (monzonite) and LBH55/1 (monzodiorite) show a strong enrichment in light rare earth elements (LREEs) and a slight enrichment in heavy rare earth elements (HREEs; Table 1). These samples have the highest positive Eu anomaly (Eu/Eu*=2.5–6.7; Fig. 7A); (b) the majority of the analysed samples [LB8 and LB16f (diorites), LI18c–f and LTa29 (monzonites) and LTo35 (monzogranite)] have overlapping,

parallel REE patterns (Fig. 7C) and an insignificant Eu anomaly (Eu/Eu* ~1). Samples LB8 and LB16f (diorites) are the exceptions, since they have a slight positive Eu/Eu* value (1.1 and 1.3, respectively). The rocks of this trend differ only in their ΣREE concentration (104–523 ppm). Similarly to the rocks of trend (a), the latter are also characterised by a marked enrichment in LREE and a minor increase in the HREE content (Table 1); whereas (c) sample LN50/1 (monzogranite) has a distinct negative Eu anomaly (Eu/Eu*=0.53; Fig. 7E). It shows modest enrichment in both the LREEs and HREEs (Table 1).

The same three trends can be distinguished in the chondrite-normalised spider diagrams (Fig. 7B, D, F): the rocks of trend (a) are characterised by elevated La, Sr, Zr, Hf, and Eu contents. Negative anomalies occur in Ta, Nd, Sm, and Tb (Fig. 7B); the rocks belonging to trend (b) show a slight positive anomaly in Nb and Ta (with some samples showing a positive Zr and Hf anomaly, as well) and a negative anomaly in U, Nd, and Tm (Fig. 7D); while trend (c) has positive Ta and Hf along with negative Nb, Sr, and Eu anomalies (Fig. 7F).

### *Mineral textures and chemistry*

Clinopyroxene

The most important textural features of the studied clinopyroxene crystals are summarised in Supplementary Table S2. The analysed clinopyroxenes were classified according to Morimoto et al. (1988) (Supplementary Fig. S1). Supplementary Table S3 contains the major and trace element compositions of the analysed crystals.

The clinopyroxenes of different textural positions in LB16m (plagioclase-bearing pyroxene hornblendite) have distinct geochemical compositions (Fig. 8; Supplementary Fig. S1): (a) groundmass clinopyroxene (Fig. 5A) is aluminian diopside ($Wo_{48}En_{37}Fs_{15}$; mg#=0.77) with a convex REE pattern (Fig. 8A). It is characterised by high Zr and Hf concentrations and low Sm, Eu, and Tb contents (Fig. 8B). Clot-forming clinopyroxene in LTa29 (monzonite; Fig. 4G) exhibits overlapping composition (Fig. 8A, B; Supplementary Fig. S1); (b) clinopyroxene in the centre of the orbicular inclusions (Figs. 4I and 5B) is diopside ($Wo_{48}En_{41}Fs_{11}$; mg#=0.85). Its REE pattern is concave (Fig. 8C); Sm, Eu, and Tb are present in high concentrations (Fig. 8D). Groundmass clinopyroxene and clinopyroxene in the centre of the orbicular inclusions in LO52/1 (lamprophyre; Fig. 4J) are of comparable composition (Fig. 8C, D; Supplementary Fig. S1).

Amphiboles

Based on their textural characteristics and geochemical composition, the examined amphiboles can be categorised as primary and secondary.

The analysed actinolite crystals are characterised by Si>7.3 and exhibit depletions in Na, K, Fe, and Ti, thereby implying
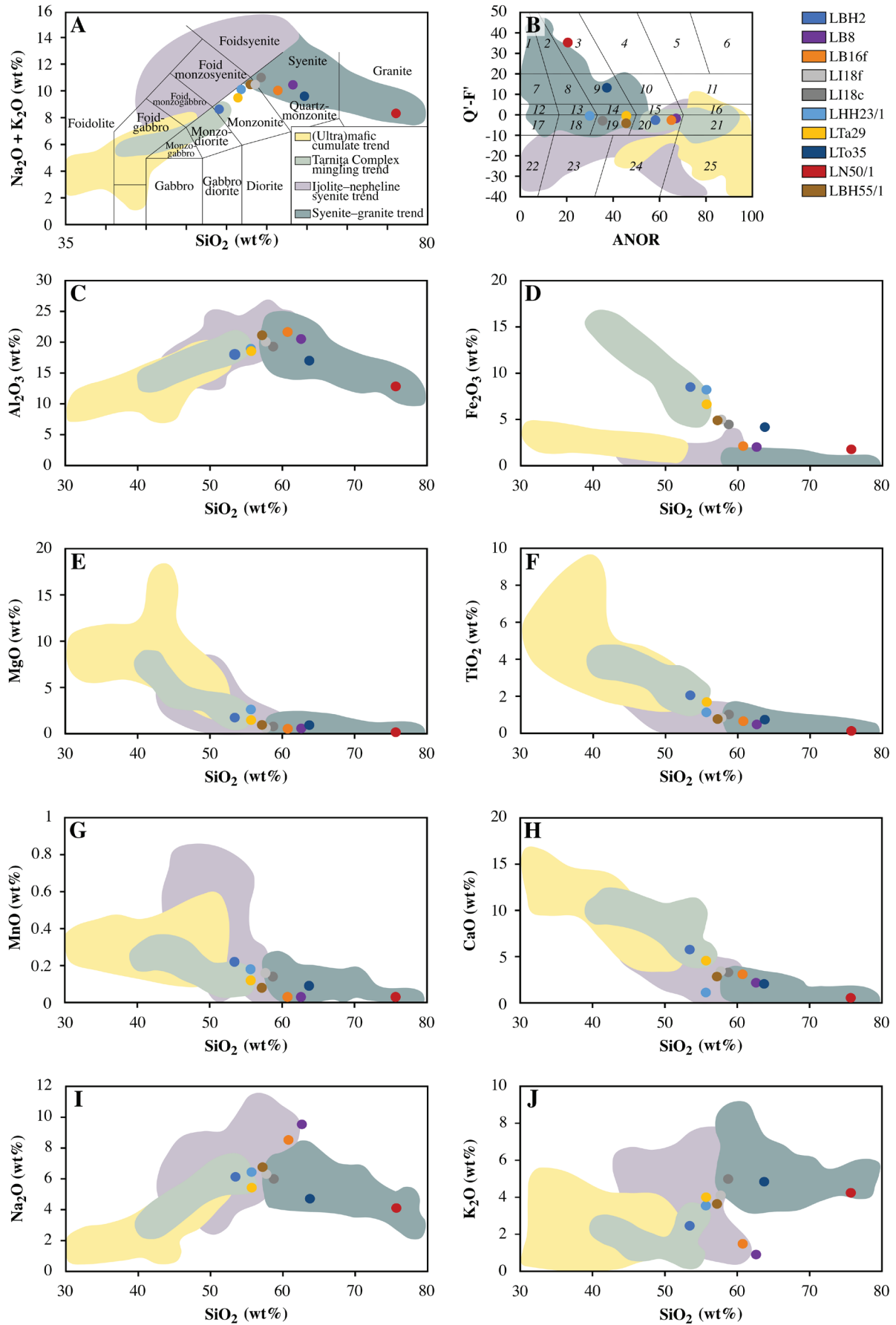
Fig. 6. A — Classification of the examined rocks based on the total alkali versus SiO$_2$ diagram (after Le Maitre et al. 2002). **B** — Classification of the studied rocks in the cation norm diagram for plutonic rocks (after Streckeisen & Le Maitre 1979). Field numbers of the diagram: 1 – alkali feldspar granite, 2 – syenogranite, 3 – monzogranite, 4 – granodiorite, 5 – tonalite, 6 – calcic tonalite, 7 – quartz alkali feldspar syenite, 8 – quartz syenite, 9 – quartz monzonite, 10 – quartz monzodiorite/monzogabbro, 11 – quartz diorite/quartz gabbro, 12 – alkali feldspar syenite, 13 – syenite, 14 – monzonite, 15 – monzodiorite/monzogabbro, 16 – diorite/gabbro, 17 – foid-bearing alkali feldspar syenite, 18 – foid-bearing syenite, 19 – foid-bearing monzonite, 20 – foid-bearing monzodiorite/monzogabbro, 21 – foid-bearing diorite/gabbro, 22 – foid syenite, 23 – foid monzosyenite, 24 – foid monzodiorite/monzogabbro, 25 – foid diorite/gabbro. **C to J** — Major element oxides plotted against SiO$_2$ for the analysed samples. Whole-rock data from Kovács & Pál-Molnár (2005), Batki et al. (2014, 2018), Pál-Molnár et al. (2015a, b), and Pál-Molnár (2021) are given for comparison, highlighted by the coloured fields. Symbol colours are the same for samples in all figures, which are given in (B).
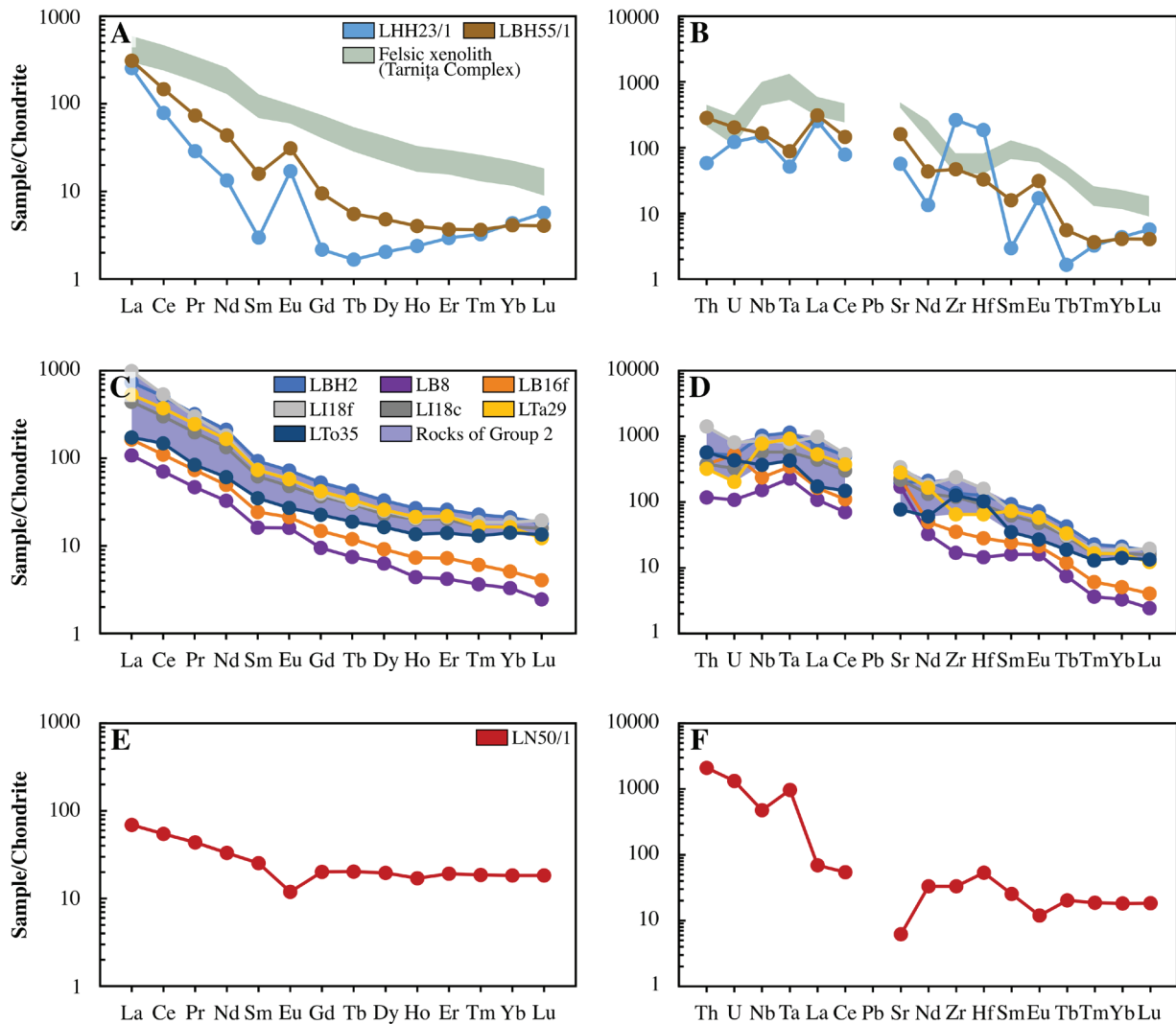
Fig. 7. Chondrite-normalised REE diagrams (left) and multielement spider diagrams (right) for the analysed rocks. For comparison, the shaded fields in (**A**) and (**B**) cover the whole-rock composition of felsic xenoliths in the Tarnița Complex from Pál-Molnár (2021). The coloured fields in (**C**) and (**D**) represent the bulk-rock composition of Group 2 rocks from this study. Normalising values are after Sun & McDonough (1989).

that they were produced by subsolidus reactions (Leake 1978; Chivas 1981; Hendry et al. 1985).

Supplementary Table S4 provides a summary of the textural characteristics of the investigated actinolites (Fig. 5C). The nomenclature of Leake et al. (1997) was applied to classify the analysed crystals. The major and trace element

compositions of the studied actinolites from sample LTa29 (monzonite) are listed in Supplementary Table S5.

Actinolite is characterised by mg# varying between 0.40 and 0.76 and the amount of Al^{IV} is 0.0–0.7 atoms per formula unit (Supplementary Fig. S2). The chondrite-normalised REE pattern of actinolite exhibits a marked
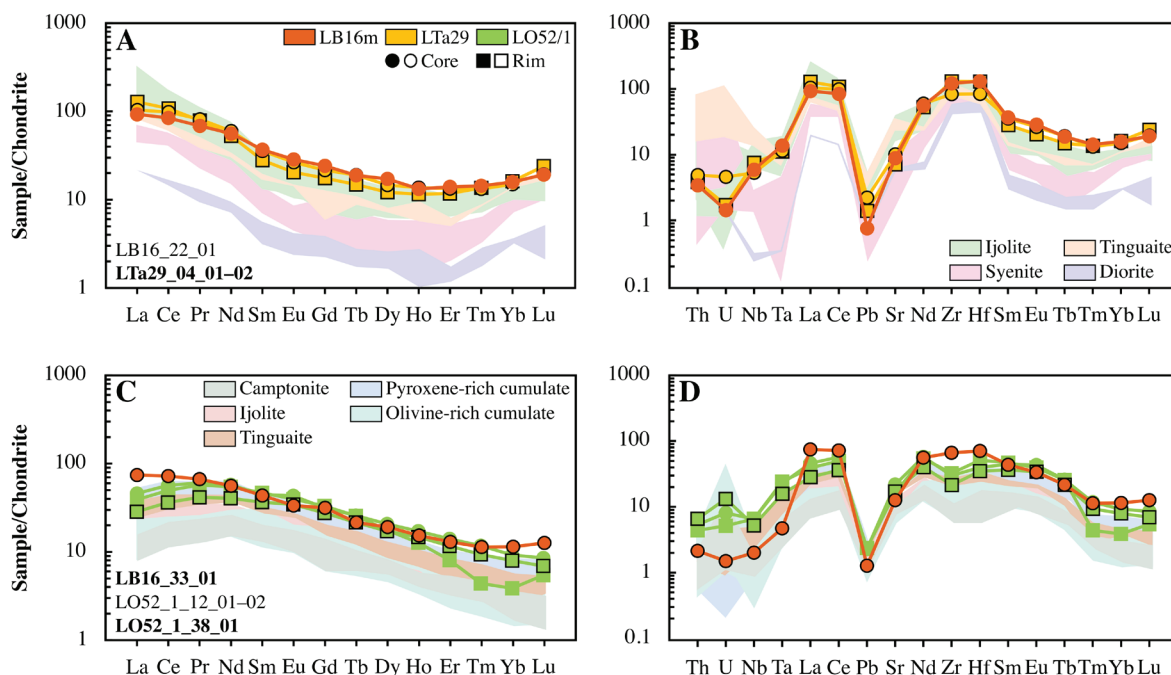
Fig. 8. Chondrite-normalised REE diagrams (left) and multielement spider diagrams (right) for selected, representative clinopyroxene compositions. **A, B** — Groundmass clinopyroxene in LB16m (plagioclase-bearing pyroxene hornblendite) and clot-forming clinopyroxene in LTa29 (monzonite). **C, D** — Orbicular inclusion-derived clinopyroxene in LB16m (plagioclase-bearing pyroxene hornblendite) along with isolated and orbicular inclusion-derived clinopyroxene in LO52/1 (lamprophyre). For comparison, the shaded fields show the compositional trends of clinopyroxenes from Batki et al. (2014, 2018) and Pál-Molnár et al. (2015a). Normalising values are according to Sun & McDonough (1989).

enrichment in LREEs and a slighter enrichment in HREEs (Fig. 9; Supplementary Table S5). The REE, as well as the trace element patterns of the analysed crystals, mostly overlap, with a general enrichment in Zr and Hf and a negative anomaly in U and Pb (Fig. 9); however, there are some clot-forming crystals with a pronounced negative Eu anomaly (Fig. 9C) or with elevated U and Pb contents (Fig. 9D).

The other group of the analysed crystals generally have a maximum Si<7.3, and they are not depleted in elements, such as Na, K, Ti, and Fe, classifying them as truly magmatic (Leake 1978).

The major textural features of the studied magmatic amphiboles are listed in Supplementary Table S6. The analysed crystals were classified according to Leake et al. (1997). The major and trace element compositions of the magmatic amphiboles are summarised in Supplementary Table S7.

The studied magmatic amphiboles exhibit significant inter-crystalline variation in major and trace element concentrations and can be classified into three separate types in line with their composition.

Type I is represented by the isolated and clot-forming amphibole (hastingsite) of LB16m (plagioclase-bearing pyroxene hornblendite; Fig. 5D). The mg# (0.5–0.6) and Al[IV] (1.8–2.0 apfu) composition of the crystals shows limited variation (Supplementary Fig. S2). The amphiboles of this group have straight REE patterns with a continuous decrease from LREEs to HREEs (Fig. 10A). Minor negative Eu (Eu/Eu* min. 0.77) and Tm, together with significant negative U and

Pb anomalies, are the characteristic features of this group (Fig. 10B). Based on its major and trace element compositions (Figs. 10A, B and 11; Supplementary Fig. S2), the groundmass and megacrystic amphibole (Fe-kaersutite and Mg-hastingsite + Fe-pargasite, respectively) of sample LO52/1 (lamprophyre) can also be ascribed to this group.

The second amphibole type (Type II) is represented by hastingsite [LBH2 (monzodiorite), LI18c–f (monzonites)], Mg-hastingsite and Fe-pargasite [LTa29 (monzonite); Fig. 5E]. The mg# varies between 0.2 and 0.5 and the amount of tetrahedral aluminium is 1.8–2.2 apfu, making it indistinguishable from Type I amphiboles (Supplementary Fig. S2). Nevertheless, this amphibole variety is characterised by a convex, U-shaped REE pattern with a marked enrichment in LREEs and a relatively limited increase in the HREE concentration (Supplementary Table S7). The amphiboles of this group show negative anomalies in U, Ta, and Pb along with positive anomalies in Nb, Zr, and Hf (Fig. 10C–H).

The third amphibole type (Type III) is characteristic of sample LTo35 (monzogranite) exclusively (Fig. 5F). It is Fe-hornblende with limited variations in the mg# (0.37–0.39) and Al[IV] (1.3–1.4 apfu) concentrations, forming a unique group in the mg# vs. Al[IV] diagram (Supplementary Fig. S2). It has a distinct, seagull-shaped REE pattern with a marked negative Eu anomaly (Fig. 10I). Pb and Zr also exhibit negative anomalies (Fig. 10J). Certain elements, for example, Nb, Ta, Nd, Sm, and Tb are present in anomalously high concentrations (Figs. 10J and 11B).

In addition, complexly-zoned amphibole crystals with zones characterised by different REE and trace element patterns and element concentrations are also present in the studied rocks (Figs. 10 and 11).

Plagioclase

The main textural characteristics of the analysed plagioclase crystals are summarised in Supplementary Table S8. The studied rocks are made up of plagioclase of variable composition (albite and oligoclase; Supplementary Fig. S3; Supplementary Table S9). It has to be noted that in some zones, the concentration of the analysed rare earth elements was below the detection limit of the analyses, resulting in anomalously low ΣREE value of these domains.

Clear groundmass plagioclase (Type I) in sample LBH2 (monzodiorite) shows no compositional zonation: its core and rim have similar major and trace element concentrations. Both zones have high Eu/Eu* values (core: 3.7 and rim: 5.3; Fig. 12A; Supplementary Table S9).

The normally-zoned plagioclase (Type II) megacryst in LTa29 (monzonite) has the highest anorthite content among the analysed plagioclase samples (Fig. 13A, B; Supplementary Fig. S3; Supplementary Table S9). The different zones are characterised by distinct REE concentrations (Fig. 12B).

Groundmass plagioclase with sericitised core (Fig. 5G) in LBH55/1 (monzodiorite) exhibits reverse zoning (Type III): its rim is relatively enriched in anorthite, FeO, and TiO$_2$

(Fig. 13A, B) and exhibits a marked positive Eu anomaly (Fig. 12C; Supplementary Table S9).

Complexly-zoned groundmass plagioclase with sericitised core (Fig. 5H) in LI18f (monzonite) is characterised by two (inner and outer) transitional zones relatively enriched in An content, FeO, TiO$_2$, and Ba (Fig. 13; Supplementary Table S9). The REEs exhibit a continuous decrease from the core towards the rim (Fig. 12D).

The core and the outer transitional zone of the complexly-zoned plagioclase with clear core in LI18f (monzonite) exhibit elevated anorthite and FeO contents, whereas the inner transitional zone and the rim are characterised by lower anorthite and FeO concentrations (Fig. 13A; Supplementary Table S9). The inner transitional zone is the most enriched in REEs and shows no Eu anomaly (Fig. 12E).

Aggregated plagioclase crystals occurring in synneusis relation exhibit distinct zoning patterns.

The complexly-zoned crystals are characterised by a transitional zone with the highest anorthite content and the highest concentrations of TiO$_2$, La, and Ce (Fig. 13B, D; Supplementary Table S9). There is no systematic difference in the REE pattern of the zones (Fig. 12F).

The normally-zoned crystals have a core with the highest anorthite content, as well as Sr and Ba concentrations among the aggregated crystals (Fig. 13B, C; Supplementary Fig. S3; Supplementary Table S9). The transitional zone is the most enriched in REEs (Fig. 12G).
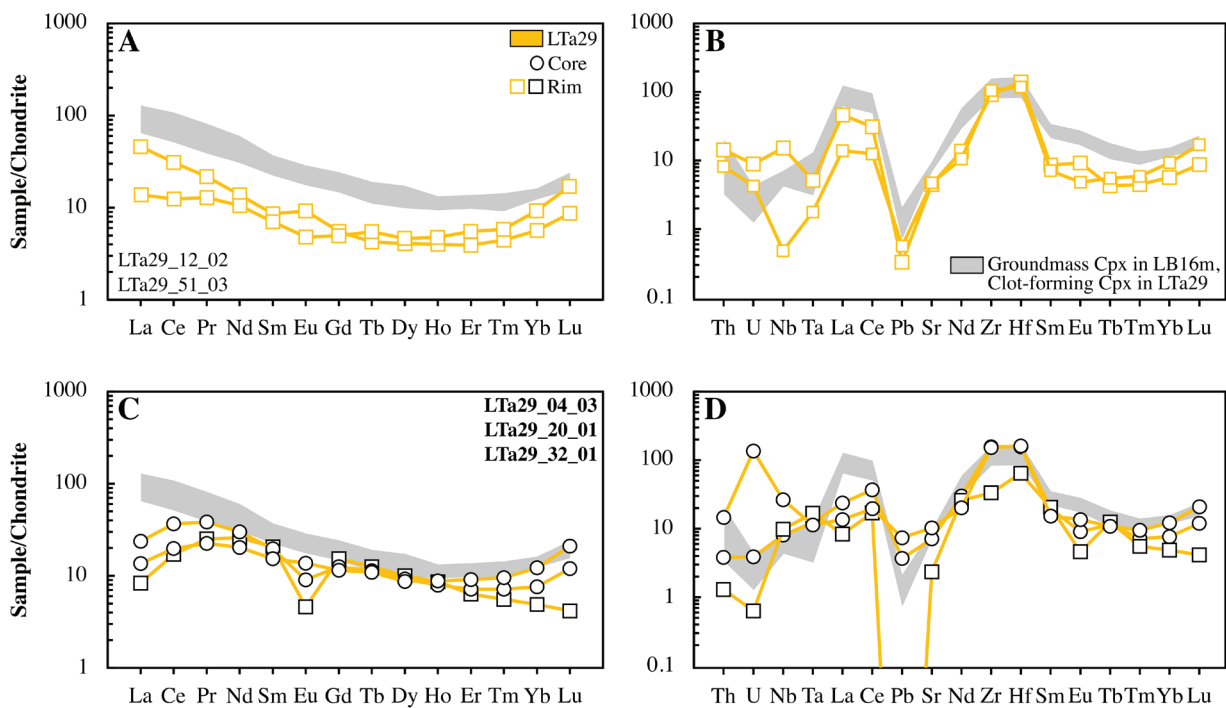

Fig. 9. Chondrite-normalised REE diagrams (left) and multielement spider diagrams (right) for the analysed actinolite crystals from sample LTa29 (monzonite). **A, B** — Compositions of the isolated, groundmass actinolite crystals. **C, D** — Composition of the clot-forming actinolites. Shaded fields show compositional trends of groundmass clinopyroxene in LB16m (plagioclase-bearing pyroxene hornblendite) and clot-forming clinopyroxene in LTa29 (monzonite) for comparison. Normalising values are according to Sun & McDonough (1989).
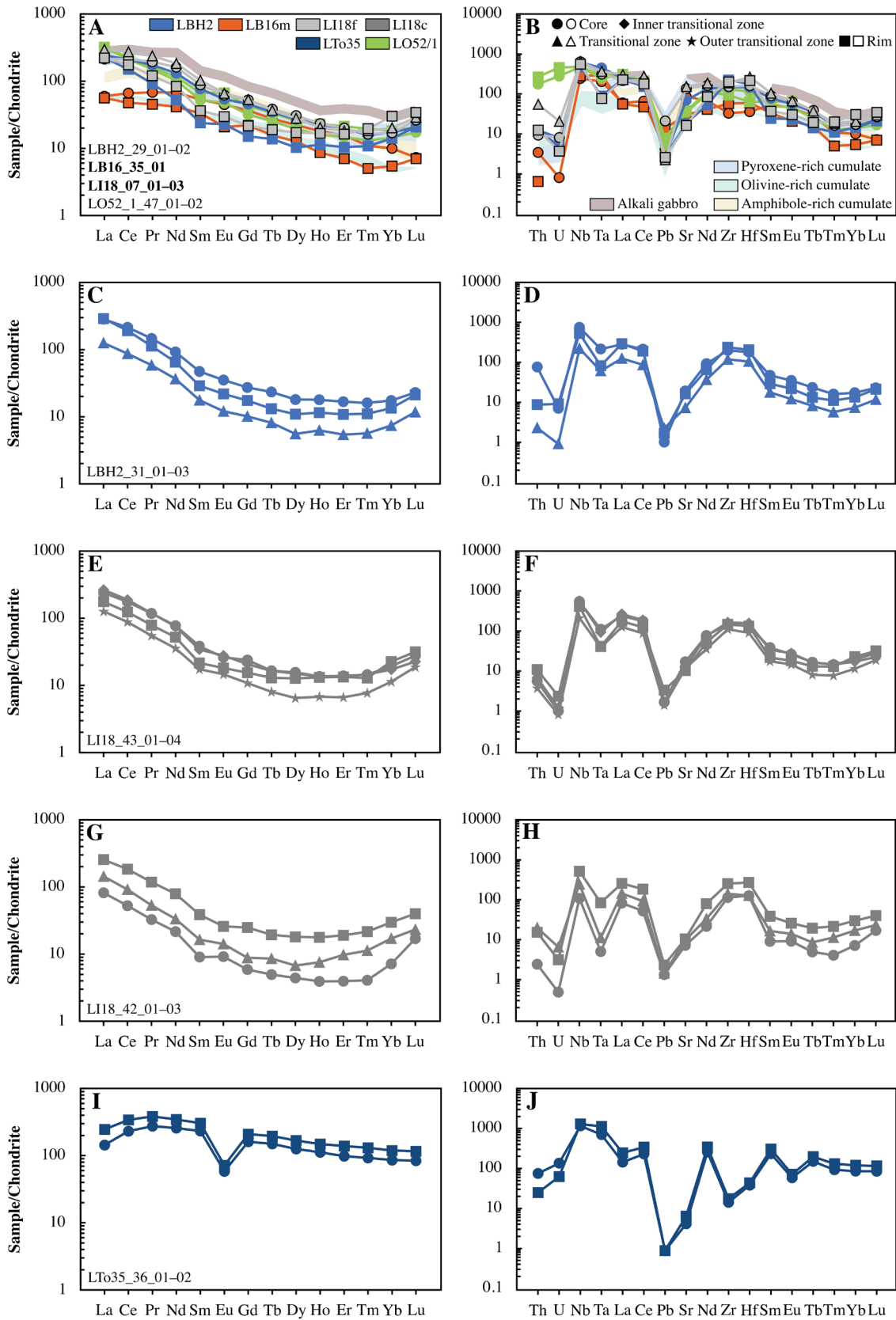
Fig. 10. Chondrite-normalised REE diagrams (left) and multielement spider diagrams (right) for representative magmatic amphibole crystals. Symbols with a black rim mark the data of clot-forming crystals. The shaded fields show compositional trends of cumulus amphibole (Pál-Molnár et al. 2015a) and amphibole of alkali gabbro (Morogan et al. 2000) for comparison. Normalising values are according to Sun & McDonough (1989).
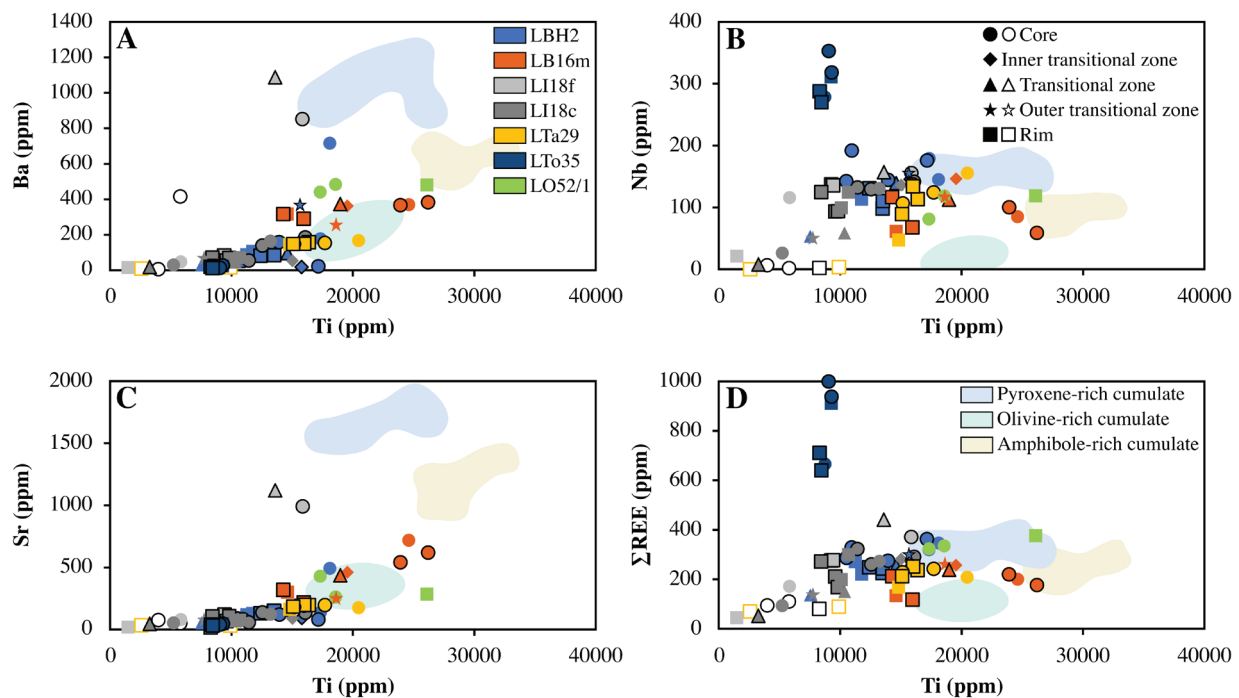
Fig. 11. Trace element compositions of the analysed amphibole crystals. Actinolite data are marked by empty symbols. The data of aggregated crystals are identified by symbols with a black rim. The shaded fields show compositional trends of cumulus amphibole (Pál-Molnár et al. 2015a) and amphibole of alkali gabbro (Morogan et al. 2000) for comparison. Normalising values are according to Sun & McDonough (1989).

The clear and unzoned crystals have a core and rim with overlapping compositions (Supplementary Table S9); nevertheless, the core is characterised by a distinct positive Eu anomaly and significantly-lower REE concentrations (Fig. 12H).

Discussion

In the following, the results of the whole-rock analyses along with clinopyroxene, amphibole, and plagioclase data will be interpreted in combination with microtextures and field observations. The aim is to provide insight into the igneous history of the DAM and identify the key processes during the evolution of the felsic suite in the northern part of the massif.

Interpretation of the whole-rock major and trace element data

When combining our new bulk-rock data with the previously-published data sets in the TAS diagram, the bulk-rock compositions of the recently analysed samples partly overlap with and connect the trends of the rocks formed by magma mingling in the Tarnița Complex [diorite (s.l.), monzodiorite, and monzonite)] and that of the syenite–granite series (Fig. 6A).

Based on their mineralogy and microtextures (Figs. 3A and 4A, B), LB8 and LB16f (diorites) were regarded as felsic cumulates (Group 1; Kiri et al. 2022). However, these samples are characterised by only a slightly positive Eu anomaly (Eu/Eu* = 1.3 and 1.1, respectively) along with a high differen-

tiation index (D.I. = 95.3 and 95.0, respectively; Table 1). Furthermore, their REE patterns overlap with those of the other analysed samples [Group 2 (Kiri et al. 2022): LBH2 (monzodiorite), LI18c–f and LTa29 (monzonites), and LTo35 (monzogranite)]; the only difference is the Eu anomaly and a slight depletion in HREEs (Fig. 7C). Therefore, based on their bulk-rock geochemical composition, LB8 and LB16f (diorites) cannot be distinguished from the above-listed samples. The advanced cumulate (Kumar & Singh 2014) nature of LB8 and LB16f (diorites) may explain the observed geochemical features.

Nevertheless, samples LHH23/1 (monzonite) and LBH55/1 (monzodiorite; Group 2; Kiri et al. 2022) exhibit a different trend (Fig. 7A). Their high Eu/Eu* (6.7 and 2.5, respectively), in accordance with the low REE concentration (ΣREE = 125 and 206 ppm, respectively), elevated La and Sr contents (Table 1), high abundance, and the microtextures of plagioclase (e.g., chain structure, impingement; Kiri et al. 2022; Fig. 4C) point to the less-differentiated, early felsic cumulate nature of these rocks (Kumar & Singh 2014). Based on the felsic xenoliths in the Tarnița Complex, Heincz et al. (2018) hypothesised the existence of a felsic cumulate pile in the DAM. Nevertheless, their bulk-rock composition (Pál-Molnár 2021) is completely different from that of LHH23/1 (monzonite) and LBH55/1 (monzodiorite; Fig. 7A, B). This implies that samples LHH23/1 (monzonite) and LBH55/1 (monzodiorite) represent the felsic cumulate phase of a magma different from that of the parental magma of the Tarnița Complex (Magma1; Batki et al. 2018).

The negative Eu anomaly (Eu/Eu*=0.5) of sample LN50/1 (monzogranite; Fig. 7E) indicates that it crystallised from a highly differentiated (D.I.=96.6), evolved melt or from an expelled residual liquid. The low REE concentration (ΣREE=114 ppm) can be attributed to crustal assimilation (Kumar & Singh 2014), and this is strongly supported by the oxygen isotope data of Ódri et al. (2020).
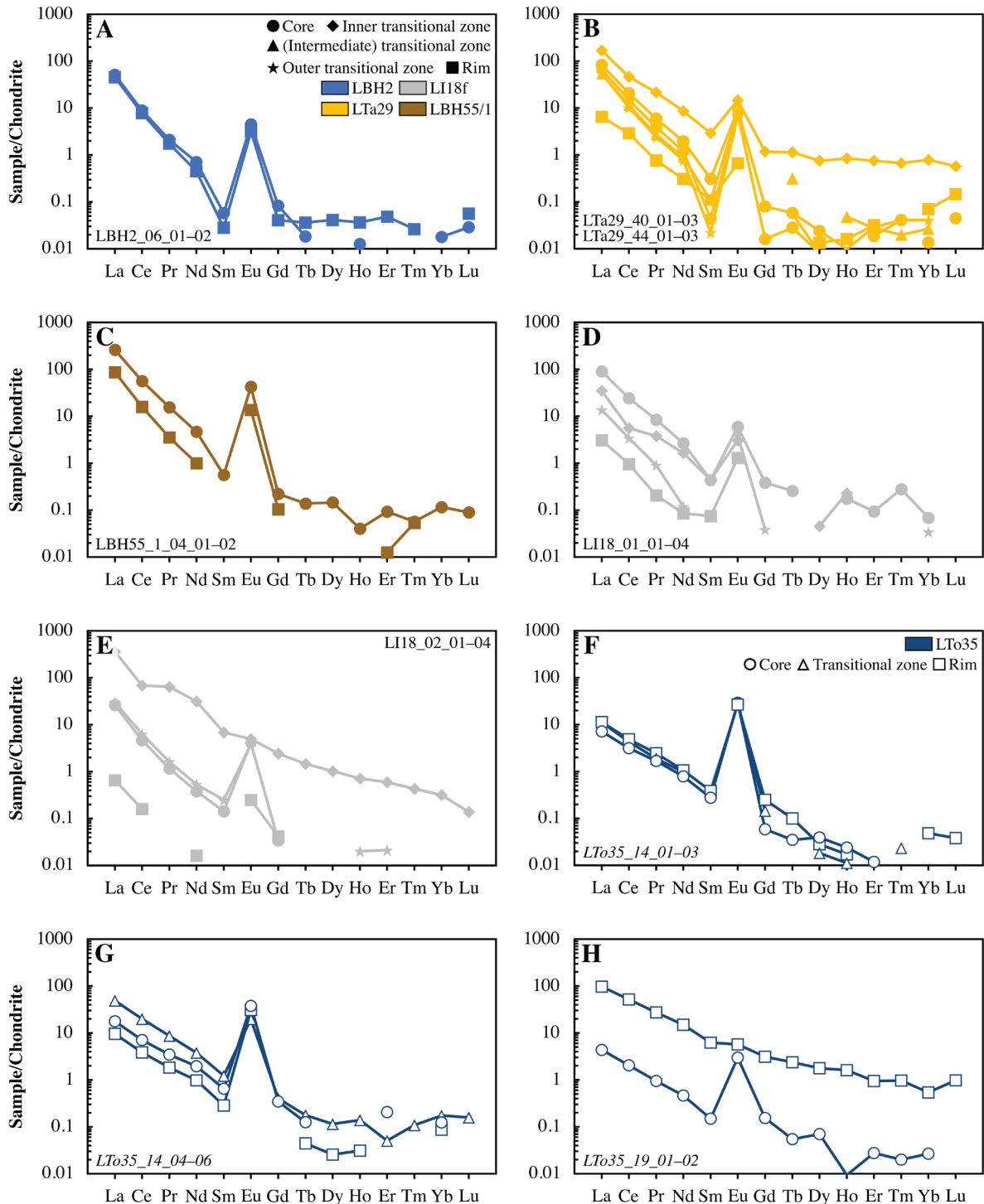
Fig. 12. Chondrite-normalised REE patterns of the analysed isolated plagioclase crystals. **A** — Clear, unzoned plagioclase; **B** — Normally-zoned megacryst; **C** — Reversely-zoned plagioclase with sericitised core; **D** — Complexly-zoned plagioclase with strongly sericitised core; **E** — Complexly-zoned plagioclase with clear core; **F** — Large, complexly-zoned plagioclase crystal with inclusion-rich and strongly sericitised core, in synneusis; **G** — Smaller-sized, normally-zoned plagioclase with sericitised core, in synneusis; **H** — Clear, unzoned plagioclase crystal, in synneusis. Normalising values are according to Sun & McDonough (1989).

Implications from the clinopyroxene data

Batki et al. (2018) identified two distinct parental magmas based on the composition of the clinopyroxene populations: Magma1 (M1), with a basanitic composition, was identified as the parental magma of the (ultra)mafic cumulates in the Tarnița Complex, whereas Magma2 (M2) evolved to a phonolitic composition, giving rise to nepheline syenite.

Isolated clinopyroxene of LB16m (plagioclase-bearing pyroxene hornblendite; Fig. 5A), as well as clustered clinopyroxene of LTa29 (monzonite; Fig. 4G), exhibit a convex REE pattern (Fig. 8A) and a trace element composition (Fig. 8B) similar to that of the green clinopyroxene crystals (classified as Type II) reported from ijolite and tinguaite dykes, as well as from diorite, and syenite (Batki et al. 2018). They are considered to be antecrysts in the tinguaite dykes, diorite, and syenite (Batki et al. 2018). Nevertheless, LB16m (plagioclase-bearing pyroxene hornblendite) has a microtexture typical of cumulates and the isolated clinopyroxene is present as a primary, cumulus mineral (autocryst). Its composition does not overlap with that of the M1-derived clinopyroxene in the orbicular inclusions (Fig. 8; Supplementary Fig. S1). Thus, LB16m (plagioclase-bearing pyroxene hornblendite) represent the cumulate phase of a different parental magma (M2; Batki et al. 2018) from which the Type II diopsides crystallised.

The clinopyroxene of the orbicular inclusions in LB16m (plagioclase-bearing pyroxene hornblendite; Fig. 5B) and LO52/1 (lamprophyre), along with the sparse isolated crystals of LO52/1, have a concave REE pattern (Fig. 8C). Pál-Molnár et al. (2015a) reported similar clinopyroxene compositions from the olivine-rich, as well as from the pyroxene-rich cumulates. The clinopyroxene described from the camptonite and tinguaite dykes, pyroxene-rich hornblendite, and ijolite enclave has very similar geochemical features (Batki et al. 2018; Fig. 8C, D). According to the classification of Batki et al. (2018), these clinopyroxenes are primitive diopsides (classified as Type I) that crystallised in a closed system from Magma1. However, in LB16m (plagioclase-bearing pyroxene hornblendite) and LO52/1 (lamprophyre), such primitive diopside crystals are present in the orbicular inclusions (Figs. 3E, F, 4I, J, and 5B). The fact that these diopsides occur in the aggregates being mantled by amphibole and biotite crystals of the host strongly implies their antecrystic origin. Periodic replenishment of M1 triggered the transport of the previously-crystallised clinopyroxenes to a new magmatic environment. Lamprophyres are feasible candidates for transporting these crystals. The mechanical break-up of the inclusions led to the fragmentation of aggregates and the scant occurrence of isolated clinopyroxene crystals in the lamprophyres.

The interaction between M1 and M2 magmas (Batki et al. 2018) is supported by the observation that orbicular inclusions with primitive diopside crystals from M1 magma were found in the M2 magma-derived LB16m rocks (plagioclase-bearing pyroxene hornblendite; Figs. 3E, 4I, 5B, and 8C–H). Clinopyroxenes of M2 were also mobilised and distributed throughout the magmatic system. This resulted in the formation of mafic mineral aggregates, some of which still preserve relics of antecrystic clinopyroxene (Batki et al. 2018; Kiri et al. 2022; Figs. 4G and 14H). Actinolite (Fig. 5C) is characterised by high mg# values (0.4–0.8) that overlap with those of the Type II diopsides (mg#=0.6–0.9). The REE and trace element patterns of actinolite (both groundmass and aggregated) in LTa29 (monzonite) are similar to those of the groundmass clinopyroxene in LB16m (plagioclase-bearing pyroxene hornblendite) and the aggregated diopside in LTa29 (monzonite; Fig. 9). This suggests that the antecrystic clinopyroxene was replaced by actinolite at lower temperatures (e.g., Vernon 1984, 1990; Castro & Stephens 1992; Hibbard 1995; Choe & Jwa 2004; Fig. 14G, H).

Implications from the amphibole data

The most important features of the analysed amphibole crystals and their interpretation are summarised in Fig. 14.

The intra-crystalline major and trace element composition of Type I amphiboles is practically identical and uniform in both LB16m (plagioclase-bearing pyroxene hornblendite; Fig. 5D) and LO52/1 (lamprophyre). Their REE and trace element patterns, as well as trace element compositions, completely overlap with those of the amphibole in olivine-rich, pyroxene-rich, and amphibole-rich cumulates (Pál-Molnár et al. 2015a), as well as in alkali gabbro (Morogan et al. 2000; Figs. 10A, B and 11). This means that although M1 and M2 magmas can be distinguished on the basis of the clinopyroxene data, the amphiboles do not show such systematic differences in their composition. Thus, the M1 and M2-derived cumulus amphibole crystals (Type I; Fig. 14A) are indiscernible from each other.

Type II amphiboles are represented by groundmass amphibole in LI18f, clot-forming amphibole in LI18c, as well as isolated and aggregated amphiboles in LTa29 (monzonites; Fig. 14B). Although their major element composition is less distinct from that of the Type I amphiboles (Supplementary Fig. S2), they are characterised by a convex REE pattern. The homogeneous internal texture and composition of these amphiboles suggest that they formed from the magma currently hosting them (Barnes et al. 2016) and were not involved in crystal transfer and/or recycling.

Groundmass and clot-forming amphiboles of LTo35 (monzogranite; Figs. 4H, 5F, and 14C), which belong to Type III, form a distinct group in the mg# *vs.* Al^{IV} diagram (Supplementary Fig. S2). Amphiboles of both textural positions exhibit a distinct, seagull-shaped REE pattern (Fig. 10I). The marked negative Eu anomaly (Eu/Eu*=min. 0.2) and the highest ΣREE concentration (1000 ppm) of all analysed crystals (Supplementary Table S7) indicate that these amphiboles are late crystallisation products (Kumar & Singh 2014). The depletions in Pb, Zr, and Eu (Fig. 10J) suggest that this amphibole variety was formed after alkaline feldspar, zircon, and plagioclase respectively (Marks et al. 2004; Barnes et al. 2016; Tang et al. 2020). The homogeneous intra-crystalline
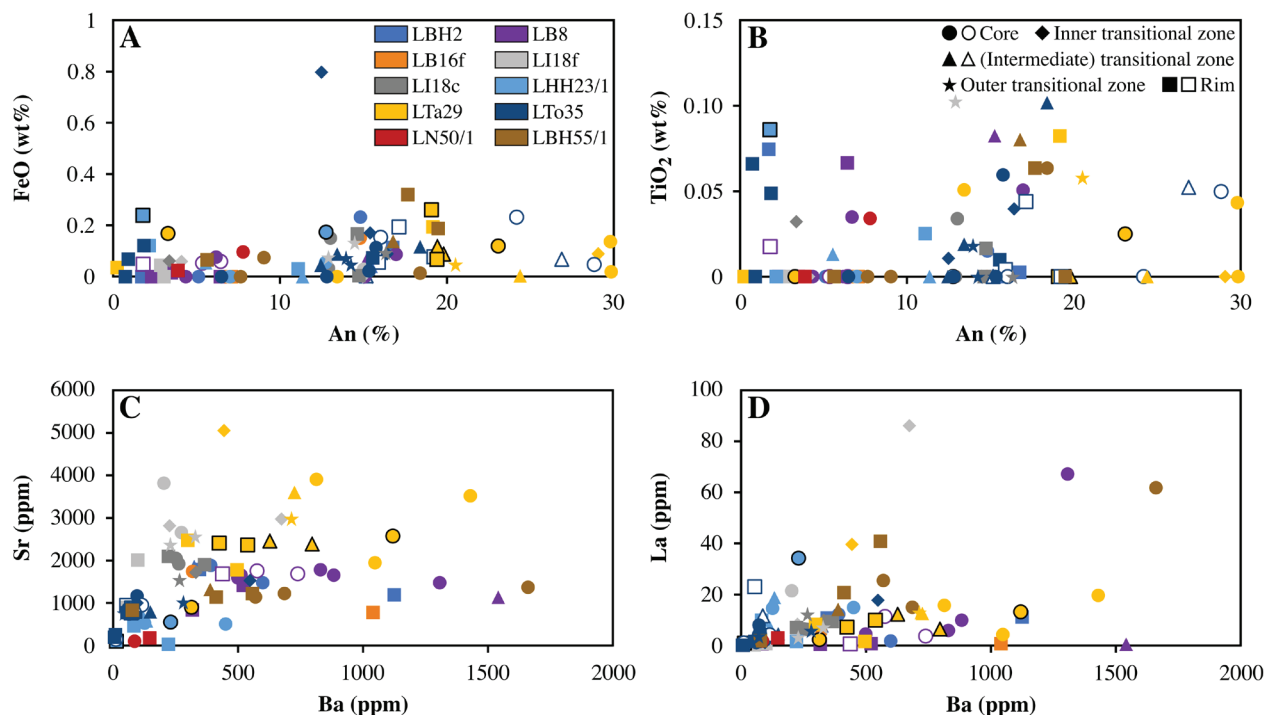
Fig. 13. Major and trace element compositions of the analysed plagioclase crystals. The composition of plagioclase crystals in synneusis is identified by empty symbols. Data of clot-forming plagioclase are marked by symbols with a black rim.

composition (Fig. 10I, J) infers that the amphiboles of this group were not involved in crystal transfer/recycling.

Some crystals show variable intra-crystalline zoning patterns and trace element concentrations (Figs. 10A–H and 11; Supplementary Fig. S2) implying their different origin and crystallisation under various circumstances. The REE patterns and the trace element composition of the core, as well as the core and transitional zone of some amphibole crystals in samples LBH2 (monzodiorite) and LI18f (monzonite), overlap with those of the Type I amphiboles of cumulate origin (Figs. 10A, B and 11). Nevertheless, their rims are characterised by a different, convex REE pattern (Fig. 10A), which is typical of Type II amphiboles. This implies that the cores and the transitional zone originated from the cumulate pile of either M1 or M2 (Wiebe et al. 1997; Klaver et al. 2017) and were dragged either by convection currents or by dykes (e.g., LI18f) that deposited them in their current, relatively more felsic environment (Bea 2010) where the rims were formed (Barnes et al. 2017; Fig. 14D). The composition of the core of the LBH2_31 (Fig. 10C, D; Supplementary Table S7), along with the core and inner transitional zone of the LI18_43 amphibole crystals (Fig. 10E, F; Supplementary Table S7), suggests that they were derived from a relatively mafic environment. Nevertheless, the absolute content of Ba, Sr, and TiO$_2$ does not approach that of the mafic cumulate-derived amphibole (Fig. 11A, C; Supplementary Table S7). Although these domains originated from a mafic magma, they represent its more evolved stage. On the other hand, the transitional zone in LBH2_31 and the outer transitional domain in LI18_43

show an abrupt decrease in the TiO$_2$, Sr, and Ba content (Fig. 11A, C; Supplementary Table S7) and imply interaction (mixing) with a more evolved magma (Barnes et al. 2017). The rims are characterised by an intermediate composition representing the present host (Figs. 10C, E and 14E). In contrast, LI18_42 in LI18c (monzonite) shows a continuous increase in ΣREE (Fig. 10G), Ba, Sr, and TiO$_2$ from the core to the rim; nevertheless, their absolute concentration is rather low (Fig. 11A, C, D; Supplementary Table S7). This suggests that the core crystallised from a felsic magma and the outer zones were formed under the influx of a magma with slightly more mafic composition (Fig. 14F).

Implications from the plagioclase data

The key characteristics of the examined plagioclase crystals and their interpretation are summarised in Fig. 14.

Regardless of their textural position (isolated or clustered), plagioclase crystals in the studied felsic rocks (even in single samples) exhibit a wide range of different zonation patterns (Fig. 12; Supplementary Fig. S3).

Ca-rich zones in feldspars (e.g., LI18_01_02–03 and LI18_02_03; Supplementary Fig. S3; Supplementary Table S9) denote a shift in their composition as a result of changing physicochemical conditions (e.g., in melt composition and/or temperature). This can be related to the transport of individual crystals into a new magmatic environment (recycling) or to the change of the physicochemical parameters around the crystal itself (Nixon & Pearce 1987; Barbarin 1990; Hattori &

	Amp type	Zonation	Texture	Features	Occurrence	Interpretation
A	Type I	Unzoned		Idiomorphic-hypidiomorphic	Ol-, Px-, Amp-rich cumulate; M2-cumulate	Cumulus phase, crystallised from M1/M2
B	Type II	Unzoned		Idiomorphic-hypidiomorphic	Monzonite, monzodiorite	Phenocryst (s.s.), crystallised from the hybrid magma
C	Type III	Unzoned		Idiomorphic-hypidiomorphic	Monzo-granite	Phenocryst (s.s.), crystallised from the fractionated hybrid magma
D	Composite	Zoned		Idiomorphic	Monzonite, monzodiorite	Core: cumulus phase from M1/M2; rim: hybrid magma
E	Composite	Complex		Idiomorphic-hypidiomorphic	Monzonite, monzodiorite	Core: fractionated foidgabbro; transition: syenite; rim: hybrid magma
F	Composite	Complex		Hypidiomorphic	Monzonite	Core: syenite magma; transition, rim: fractionated foidgabbro
G	Actinolite	Unzoned		Xenomorphic	Monzonite	Secondary, after Cpx (Type II)
H	Mafic clot	-		Stubby to slightly elongated; size: ~ 5 mm; minerals: Cpx (Type II), Amp (Type II and Act)	Monzonite	Amp (Type II and Act) on Cpx (Type II) antecryst nucleus

	Pl type	Zonation	Texture	Features	Occurrence	Interpretation
I	Type I	Unzoned		Hypidiomorphic-xenomorphic	Monzonite, monzodiorite	Phenocryst (s.s.), crystallised from the hybrid magma
J	Type II	Normal		Idiomorphic-hypidiomorphic; clear or sericitised core	Diorite (s.l.), monzonite, monzogranite	Core: fractionated foidgabbro; rim: (fractionated) hybrid magma
K	Type III	Reverse		Idiomorphic-hypidiomorphic; sericitised core	Monzonite, monzodiorite	Core: syenite magma; rim: fractionated foidgabbro
L	Composite	Complex		Idiomorphic-hypidiomorphic; sericitised core	Diorite (s.l.), monzonite, monzodiorite, monzogranite	Core: syenite magma; transition: fractionated foidgabbro; rim: hybrid magma
M	Composite	Complex		Idiomorphic-hypidiomorphic; clear core, clear or sericitised inner transition ± hybrid rim	Monzonite, monzogranite	Core+outer transition: fractionated foid-gabbro; inner transition+rim: hybrid
N	Felsic clot	-		Stubby to elongated; size: max. 5 mm; minerals: Pl (Type I and II)	Monzogranite	Crystals from different regions of the system in synneusis orientation
O	Felsic cumulate I	-		Whole-rock composition shows no Eu-anomaly	Tarniţa Complex	Xenolith, entrained in solid state; felsic cumulate of M1
P	Felsic cumulate II	-		Whole-rock composition shows marked positive Eu-anomaly	Bordea Creek, Holoşag Creek	Felsic cumulate of M2

Fig. 14. Summary of the analysed amphibole and plagioclase crystals with respect to their zonation, texture and occurrence as well as the interpretation of their origin and crystallisation history. Abbreviations: Act – actinolite, Amp – amphibole, Cpx – clinopyroxene, Ol – olivine; M1 – Magma1, M1a – Magma1a, M2 – Magma2, M2a – Magma2a, M2b – Magma2b, referring to the magmatic environments in the Ditrău Alkaline Massif.

Sato 1996; Grogan & Reavy 2002; Kahl et al. 2011, 2015, 2017). Intermittent recharge of mafic magmas results in the coupled increase in the MgO, FeO, TiO_2, Sr, Ba, La, Ce, and anorthite content of plagioclase (Hattori & Sato 1996; Słaby et al. 2002, 2007, 2011; Smith et al. 2009). Nevertheless, no evidence of such a process has been identified (e.g., mafic microgranular enclave swarms in the felsic suite in the northern part of the DAM), and none of the analysed plagioclase compositional zones show such systematic, concurrent geochemical trends (Fig. 13; Supplementary Table S9). This inconsistency could be explained by the nature of the interacting end-members. Differentiation may fractionate mafic magmas towards intermediate, so that the concentration of the above-mentioned elements gradually decreases. Mixing with a differentiated, more evolved mafic magma – which still preserves some of its typical mafic features (e.g., high mg#, Ba, Sr, and TiO_2 contents; Coint et al. 2013) – could result in the observed geochemical patterns. The composition of the rims corresponds to that of their respective, evolved hybrid host (Figs. 12D, E and 14L, M).

Synneusis texture (Fig. 4D) indicates a period of turbulence and stirring in the system (Brown 1956; Brothers 1964; Vance 1969; Grogan & Reavy 2002). Plagioclase crystals occurring in synneusis relation (e.g., LTo35_14 and LTo35_19) are characterised by different zoning patterns (Fig. 12F–H; Supplementary Fig. S3; Supplementary Table S9), proving their distinct origin and crystallisation history within the magmatic system (Fig. 14N).

Implications for the evolution of the Ditrău Alkaline Massif

The rocks of the DAM were formed by the emplacement and interaction of different magma batches in an open-system igneous environment (e.g., Batki et al. 2018; Heincz et al. 2018; Ódri et al. 2020; Fig. 15). The clinopyroxene-based study of Batki et al. (2018) has confirmed the presence of two, compositionally-different parental magmas and associated evolutional trends. Magma1 of basanitic composition (Batki et al. 2018) fractionated towards monzodioritic/monzonitic composition. Not only mafic, but also felsic roof cumulates were formed from this magma (Pál-Molnár et al. 2015a; Heincz et al. 2018; Fig. 15A, B, I). Intermittent replenishment by magmas of higher temperature and less-evolved composition produced mafic microgranular enclaves in the Tarnița Complex. Concurrent turbulence dragged and dispersed the felsic cumulate fragments into the lower part of the system (Heincz et al. 2018; Figs. 14O and 15J).

The evolution of Magma2 resulted in the formation of a phonolitic magma, parental to nepheline syenite (Batki et al. 2018; Fig. 15D). The bulk-rock composition of the Magma1-derived felsic xenoliths in the Tarnița Complex (Pál-Molnár 2021) is completely different from that of LHH23/1 (monzonite) and LBH55/1 (monzodiorite; Fig. 7A, B). This implies that these samples were formed concurrently from Magma2 in those areas where the convection was restricted, and the thermal and compositional gradients diminished (Figs. 14P and 15C).

The composition of the groundmass clinopyroxene in LB16m (plagioclase-bearing pyroxene hornblendite; Fig. 8A, B) and the texture of the rock (Fig. 3E) implies that this sample could be the so-far unrecognised cumulate phase of M2 (Batki et al. 2018; Fig. 15C). The orbicular inclusions of LB16m (Figs. 3E and 4I) contain clinopyroxene crystals (Fig. 5B) of a composition overlapping with that of the cumulus clinopyroxene of M1 (Fig. 8C, D). This suggests that an interaction between the two magma bodies took place in the deeper sections of the igneous system (Fig. 15C, D). Tinguaite with ijolite enclaves was formed by the magma mingling of the fractionated derivatives of M1 and M2 (Fig. 15E–G).

During the emplacement of M2 magma, excess heat caused partial melting in the country rocks, which resulted in the formation of a syenitic magma (Hildreth & Moorbath 1988; Bergantz 1989; Fig. 15H). As Ódri et al. (2020) suggested, the proportion of the upper crustal material could be approximately 20–25 % in syenite. Abundant syenite dykes (e.g., crosscutting the Tarnița Complex; Fig. 2A) support the presence of a syenitic magma.

In the TAS diagram, the bulk-rock compositions of the recently-analysed samples partly overlap with and connect the trend of the rocks formed by magma mingling in the Tarnița Complex and that of the syenite–granite series (Fig. 6A). There is a distinct, widespread group of amphiboles (Type II) occurring in almost all of the analysed felsic samples (Figs. 5E and 14B). However, these rocks also contain zoned amphibole crystals (Fig. 14D), and the composition of their core resembles that of the amphibole in cumulate rocks (Type I) of either M1 (Pál-Molnár et al. 2015a) or M2 (Fig. 10A, B), whereas the composition of their rims overlaps with that of the Type II amphiboles. The amphibole and plagioclase crystals are diverse in terms of their size along with their inter- and intracrystalline zoning patterns (Figs. 10, 11, 12, and 13; Supplementary Figs. S2 and S3). These features indicate the hybrid nature of the studied rocks (Słaby et al. 2007; Barnes et al. 2016) and strongly suggest that they were formed by the interaction (magma mixing) of the syenitic magma and the fractionated (most likely intermediate) derivative of M1 (Fig. 15K), with the latter still preserving some of its pristine mafic features (e.g., relatively high mg#, TiO_2, Sr, and Ba contents; Coint et al. 2013). The interaction between the end-members with comparable rheological properties, temperature, and relatively similar, felsic composition resulted in thorough mixing rather than mingling (Sparks & Marshall 1986; Bateman 1995; Poli et al. 1996; Ubide et al. 2014b). This could explain the absence of mafic microgranular enclaves and other, outcrop and macro-scale evidence of open-system igneous processes in the northern part of the massif (between the Tarnița and Turcului Creeks). This region [exemplified by samples LBH2 (monzodiorite), LI18c–f, and LTa29 (monzonites)] represents the early stage of the interaction (Bateman 1995) and/or the structurally-higher section of the hybrid zone, where low crystallinity and convection favoured thorough mixing. Along the Ditrău–Hagota road (central part of the DAM), magma mingling is exposed, which
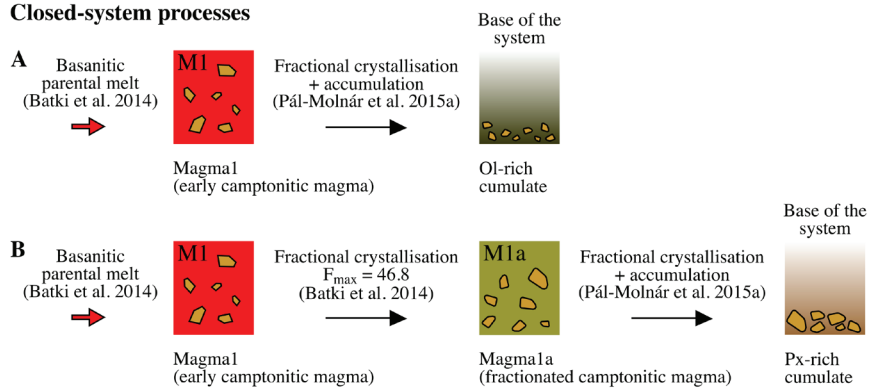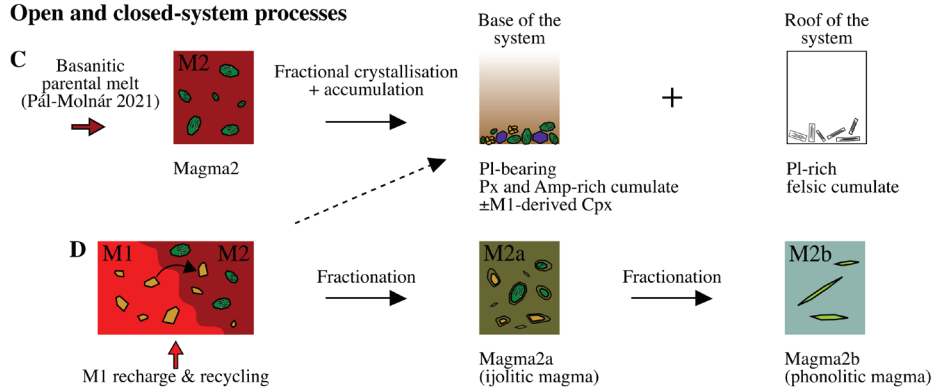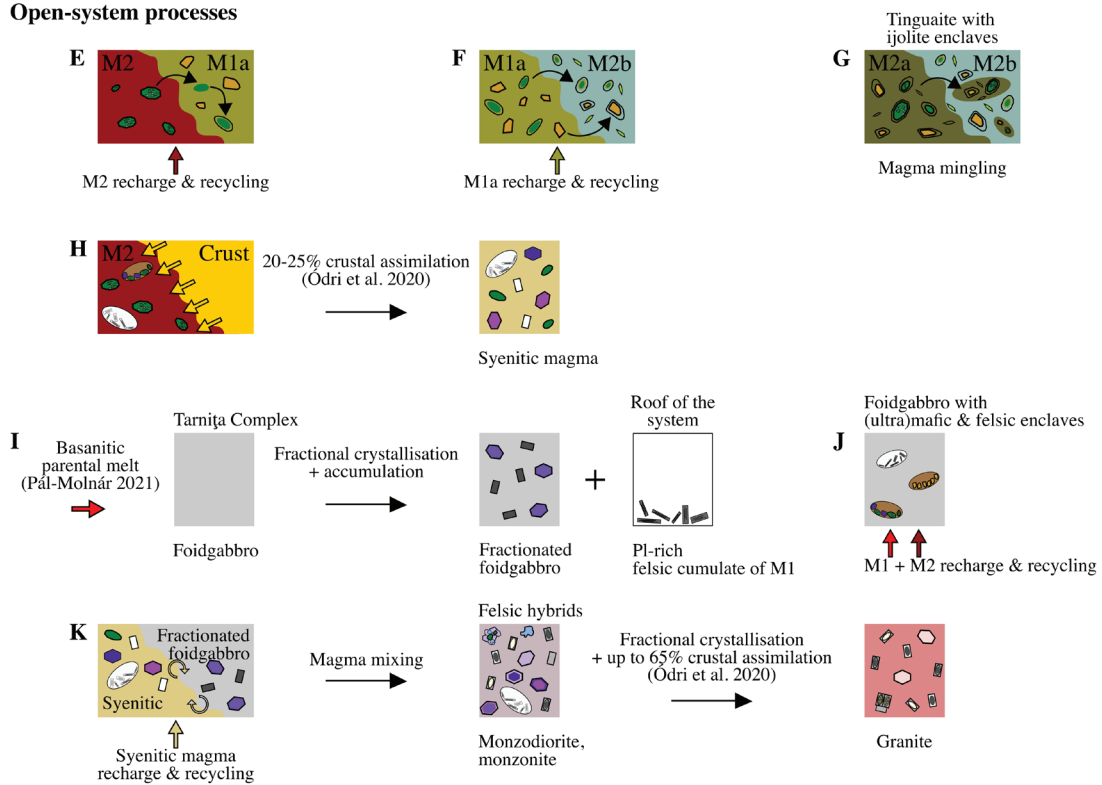
Fig. 15. Schematic emplacement model for the Ditrău Alkaline Massif (modified after Batki et al. 2018). The relative size of the structural and textural elements is not illustrated to scale. Mineral illustrations and abbreviations of the magmatic environments can be found in Fig. 14 and in Batki et al. (2018). See text for details.

is evidenced by mafic enclaves and large mafic, as well as felsic cumulate blocks (Fig. 2B–D). This was formed subsequently in the thermal history of the massif (Bateman 1995) and/or it could be the lower part of the hybrid zone, where the locked crystal mush hindered magmatic stirring and resulted in structural inhomogeneities.

Fractionation of the hybrid magma (Campos et al. 2002) resulted in the formation of amphibole autocrysts/phenocrysts of uniform composition (Type II; Fig. 14B). Their homogeneous internal texture and composition (Fig. 5E) imply that they were formed from the magma currently hosting them (Barnes et al. 2016) and were not involved in crystal transfer and/or recycling.

Amphiboles of LTo35 (monzogranite; Figs. 4H, 5F, 10I, J, and 14C; Supplementary Fig. S2) crystallised from an evolved magma batch that developed from further fractionation of the hybrid magma (Campos et al. 2002) and simultaneous assimilation of additional crustal material (Fig. 15K). The latter is supported by the findings of Ódri et al. (2020), according to which quartz monzonite contains 50 % lower crustal material, while granite is characterised by 35–65 % upper crustal contribution.

The intrusion of lamprophyre, ijolite, tinguaite, and (nepheline)syenite dykes (Fig. 2A, E) marked the last stage of the igneous activity. They represent M1, M2, and the syenitic melt respectively.

Conclusions

Previously, the felsic rocks of the northern part of the Ditrău Alkaline Massif (Eastern Carpathians, Romania) were regarded as a homogeneous, uniform assemblage. However, there is great micro-scale diversity (e.g., mafic clots, felsic aggregates, distinct zonation patterns of adjacent plagioclase crystals) in the felsic suite north of the Jolotca Creek valley.

The whole-rock major and trace element data support the previous hypotheses deduced from petrographic observations and prove the existence of two, compositionally-different felsic cumulate piles in the DAM.

Bulk-rock data, amphibole, and plagioclase compositions attest to the hybrid nature of the majority of the felsic rocks occurring in the northern part of the massif. Crystal transfer and recycling, as well as hybridisation were unravelled by the unique composition in the different zones of amphibole and plagioclase crystals. All these features suggest that the studied rocks were formed by the mixing of magmas with relatively similar composition, temperature, and rheological properties.

References

Anderson A.T. 1984: Probable relation between plagioclase zoning and magma dynamics, Fuego Volcano, Guatemala. *American Mineralogist* 69, 660–676.

Balintoni I. 1997: Geotectonica terenurilor metamorfice din România (Geotectonics of metamorphic terrains in Romania). *Carpatica*, Cluj Napoca (in Romanian).

Balintoni I., Balica C., Ducea M.N. & Hann H.-P. 2014: Peri-Gondwanan terranes in the Romanian Carpathians: A review of their spatial distribution, origin, provenance, and evolution. *Geoscience Frontiers* 5, 395–411. https://doi.org/10.1016/j.gsf.2013.09.002

Barbarin B. 1990: Plagioclase xenocrysts and mafic magmatic enclaves in some granitoids of the Sierra Nevada Batholith, California. *Journal of Geophysical Research* 95, B11, 17747–17756. https://doi.org/10.1029/JB095iB11p17747

Barnes C.G., Memeti V. & Coint N. 2016: Deciphering magmatic processes in calc-alkaline plutons using trace element zoning in hornblende. *American Mineralogist* 101, 328–342. https://doi.org/10.2138/am-2016-5383

Barnes C.G., Berry R., Barnes M.A. & Ernst W.G. 2017: Trace element zoning in hornblende: Tracking and modeling the crystallization of a calc-alkaline arc pluton. *American Mineralogist* 102, 2390–2405. https://doi.org/10.2138/am-2017-6063

Bateman R. 1995: The interplay between crystallization, replenishment and hybridisation in large felsic magma chambers. *Earth-Science Reviews* 39, 91–106. https://doi.org/10.1016/0012-8252(95)00003-S

Batki A., Pál-Molnár E., Dobosi G. & Skelton A. 2014: Petrogenetic significance of ocellar camptonite dykes in the Ditrău Alkaline Massif, Romania. *Lithos* 200–201, 181–196. https://doi.org/10.1016/j.lithos.2014.04.022

Batki A., Pál-Molnár E., Jankovics M.É., Kerr A.C., Kiss B., Markl G., Heincz A. & Harangi Sz. 2018: Insights into the evolution of an alkaline magmatic system: An in situ trace element study

of clinopyroxenes from the Ditrău Alkaline Massif, Romania. *Lithos* 300–301, 51–71. https://doi.org/10.1016/j.lithos.2017.11.029

Baxter S. & Feely M. 2002: Magma mixing and mingling textures in granitoids: examples from the Galway Granite, Connemara, Ireland. *Mineralogy and Petrology* 76, 63–74. https://doi.org/10.1007/s007100200032

Bea F. 2010: Crystallization dynamics of granite magma chambers in the absence of regional stress: Multiphysics modeling with natural examples. *Journal of Petrology* 51, 1541–1569. https://doi.org/10.1093/petrology/egq028

Bergantz G.W. 1989: Underplating and partial melting: Implications for melt generation and extraction. *Science* 245, 1093–1095.

Blundy J.D. & Shimizu N. 1991: Trace element evidence for plagioclase recycling in calc-alkaline magmas. *Earth and Planetary Science Letters* 102, 178–197. https://doi.org/10.1016/0012-821X(91)90007-5

Blundy J.D. & Wood B.J. 1991: Crystal-chemical controls on the partitioning of Sr and Ba between plagioclase feldspar, silicate melts, and hydrothermal solutions. *Geochimica et Cosmochimica Acta* 55, 193–209. https://doi.org/10.1016/0016-7037(91)90411-W

Brothers R.N. 1964: Petrofabric analyses of Rhum and Skaergaard layered rocks. *Journal of Petrology* 6, 255–274. https://doi.org/10.1093/petrology/5.2.255

Brown G.M. 1956: The layered ultrabasic rocks of Rhum, Inner Hebrides. *Philosophical Transactions of the Royal Society of London, Series B, Biological Sciences* 240, 1–53. https://doi.org/10.1098/rstb.1956.0011

Campos T.F.C., Neiva A.M.R. & Nardi L.V.S. 2002: Geochemistry of the Rio Espinharas hybrid complex, northeastern Brazil. *Lithos* 64, 131–153. https://doi.org/10.1016/S0024-4937(02)00199-8

Castro A. & Stephens W.E. 1992: Amphibole-rich polycrystalline clots in calc-alkaline granitic rocks and their enclaves. *Canadian Mineralogist* 30, 1093–1112.

Chivas A.R. 1981: Geochemical evidence for magmatic fluids in porphyry copper mineralization. *Contributions to Mineralogy and Petrology* 78, 389–403. https://doi.org/10.1007/BF00375201

Choe W.H. & Jwa Y.J. 2004: Petrological and geochemical evidences for magma mixing in the Palgongsan Pluton. *Geosciences Journal* 8, 343–354. https://doi.org/10.1007/BF02910470

Coint N., Barnes C.G., Yoshinobu A.S., Barnes M.A. & Buck S. 2013: Use of trace element abundances in augite and hornblende to determine the size, connectivity, timing, and evolution of magma batches in a tilted batholith. *Geosphere* 9, 1747–1765. https://doi.org/10.1130/GES00931.1

Costa F. 2021: Clocks in magmatic rocks. *Annual Review of Earth and Planetary Sciences* 49, 231–252. https://doi.org/10.1146/annurev-earth-080320-060708

Cross W., Iddings J.P., Pirrson L.V. & Washington H.S. 1902: A quantitative chemicomineralogical classification and nomenclature of igneous rocks. *Journal of Geology* 10, 555–590.

Deering C.D. & Bachmann O. 2010: Trace element indicators of crystal accumulation in silicic igneous rocks. *Earth and Planetary Science Letters* 297, 324–331. https://doi.org/10.1016/j.epsl.2010.06.034

Ginibre C., Worner G. & Kronz A. 2002: Minor- and trace-element zoning in plagioclase: implications for magma chamber processes at Parinacota volcano, northern Chile. Contributions to Mineralogy and Petrology 143, 300–315. https://doi.org/10.1007/s00410-002-0351-z

Grogan S.E. & Reavy R.J. 2002: Disequilibrium textures in the Leinster Granite Complex, SE Ireland: evidence for acid-acid magma mixing. *Mineralogical Magazine* 66, 929–939. https://doi.org/10.1180/0026461026660068

Gros K., Słaby E., Birski L., Kozub-Budzyń G. & Sláma J. 2020: Geochemical evolution of a composite pluton: insight from major and trace element chemistry of titanite. *Mineralogy and Petrology* 114, 375–401. https://doi.org/10.1007/s00710-020-00715-x

Haas J., Budai T., Csontos L., Fodor L. & Konrád Gy. 2010: Pre-Cenozoic geological map of Hungary 1:500 000. *Geological Institute of Hungary*, Budapest.

Hattori K. & Sato H. 1996: Magma evolution recorded in plagioclase zoning in 1991 Pinatubo eruption products. *American Mineralogist* 81, 982–994. https://doi.org/10.2138/am-1996-7-820

Heincz A., Pál-Molnár E., Kiss B., Batki A., Almási E.E. & Kiri L. 2018: Nyílt rendszerű magmás folyamatok: magmakeveredés, kristálycsere, kumulátum recirkuláció nyomai a Ditrói Alkáli Masszívumban (Orotva, Románia) [Open-system magmatic processes: magma mingling, crystal transfer and cumulate recycling in the Ditrău Alkaline Massif (Jolotca, Romania)]. *Földtani Közlöny* 148, 125–142 (in Hungarian). https://doi.org/10.23928/foldt.kozl.2018.148.2.125

Hendry D.A.F., Chivas A.R., Long J.V.P. & Reed S.J.B. 1985: Chemical differences between minerals from mineralizing and barren intrusions from some North American porphyry copper deposits. *Contributions to Mineralogy and Petrology* 89, 317–329. https://doi.org/10.1007/BF00381554

Hibbard M.J. 1981: The magma mixing origin of mantled feldspars. *Contributions to Mineralogy and Petrology* 76, 158–170. https://doi.org/10.1007/BF00371956

Hibbard M.J. 1995: Petrography to petrogenesis. *Prentice Hall*, Englewood Cliffs, New Jersey, 1–587.

Hildreth W. & Moorbath S. 1988: Crustal contributions to arc magmatism in the Andes of Central Chile. *Contributions to Mineralogy and Petrology* 98, 455–489. https://doi.org/10.1007/BF00372365

Huang F., Scaillet B., Wang R., Erdmann S., Chen Y., Faure M., Liu H., Xie L., Wang B. & Zhu J. 2019: Experimental constraints on intensive crystallization parameters and fractionation in A-type granites: a case study on the Qitianling Pluton, South China. *Journal of Geophysical Research, Solid Earth* 124, 10132–10152. https://doi.org/10.1029/2019JB017490

Jakab Gy. 1998: Geologia Masivului alcalin de la Ditrău [Geology of the Alkaline Massif of Ditrău]. *Pallas-Akademia*, Miercurea-Ciuc (in Romanian).

Kahl M., Chakraborty S., Costa F. & Pompilio M. 2011: Dynamic plumbing system beneath volcanoes revealed by kinetic modelling and the connection to monitoring data: An example from Mt. Etna. *Earth and Planetary Science Letters* 308, 11–22. https://doi.org/10.1016/j.epsl.2011.05.008

Kahl M., Chakraborty S., Pompilio M. & Costa F. 2015: Constraints on the nature and evolution of the magma plumbing system of Mt. Etna volcano (1991–2008) from a combined thermodynamic and kinetic modelling of the compositional record of minerals. *Journal of Petrology* 56, 2025–2068. https://doi.org/10.1093/petrology/egv063

Kahl M., Viccaro M., Ubide T., Morgan D.J. & Dingwell D.B. 2017: A branched magma feeder system during the 1669 eruption of Mt. Etna: evidence from a time-integrated study of zoned olivine phenocryst populations. *Journal of Petrology* 58, 443–472. https://doi.org/10.1093/petrology/egx022

Kiri L., Szemerédi M. & Pál-Molnár E. 2022: Petrographic evidences of open-system magmatic processes in the felsic rocks of the northern part of the Ditrău Alkaline Massif (Eastern Carpathians, Romania). *Central European Geology* 65, 49–76. https://doi.org/10.1556/24.2022.00113

Klaver M., Matveev S., Berndt J., Lissenberg C.J. & Vroon P.Z. 2017: A mineral and cumulate perspective to magma differentiation at Nisyros volcano, Aegean arc. *Contributions to Mineralogy and Petrology* 172, 95. https://doi.org/10.1007/s00410-017-1414-5
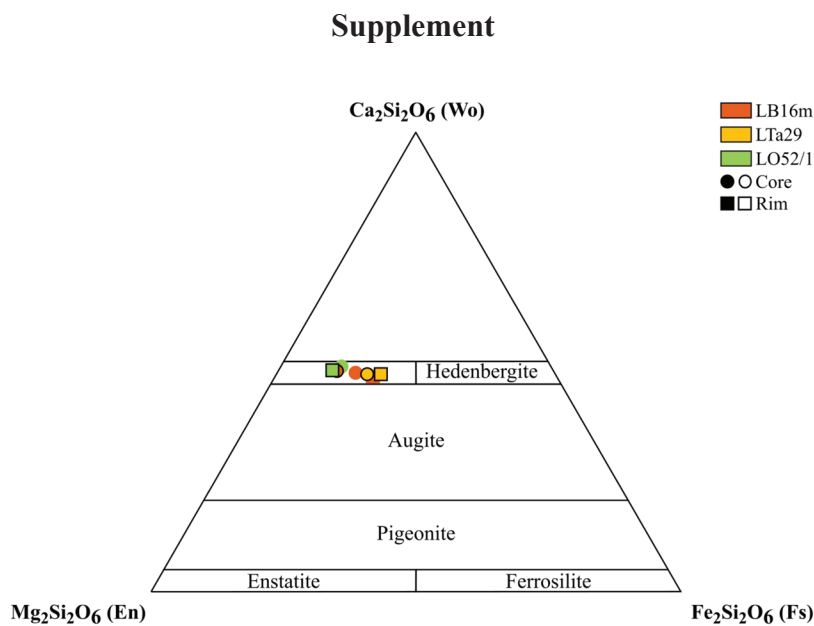
Klötzli U., Burda J., Li Q.-L., Liu Y., Jakab Gy., Ionescu L. & Tibuleac P. 2022: Petrochronological evidence for a three-stage magmatic evolution of the youngest nepheline syenites from the Ditrău Alkaline Massif, Romania. *Minerals* 12, 657. https://doi.org/10.3390/min12050657

Kovács G. & Pál-Molnár E. 2005: A Ditrói alkáli masszívum granitoid kőzeteinek petrogenezise [Petrogenesis of the granitoid rocks of the Ditrău Alkaline Massif (Transylvania, Romania)]. *Földtani Közlöny* 135, 121–143 (in Hungarian).

Kräutner H.G. & Bindea G. 1995: The Ditrău alkaline intrusive complex and its geological environment. *Romanian Journal of Mineralogy* 77, 1–44.

Kräutner H.G. & Bindea G. 1998: Timing of the Ditrău alkaline intrusive complex (Eastern Carpathians, Romania). *Slovak Geological Magazine* 4, 213–221.

Kumar S. & Singh R.N. 2014: Modelling of magmatic and allied processes. *Springer International Publishing*, Switzerland, 1–240. https://doi.org/10.1007/978-3-319-06471-0

Le Maitre R.W., Streckeisen A., Zanettin B., Le Bas M.J., Bonin B., Bateman P., Bellieni G., Dudek A., Efremova S., Keller J., Lameyre J., Sabine P.A., Schmid R., Sørensen H. & Woolley A.R. 2002: Igneous rocks: A classification and glossary of terms. Recommendations of the IUGS Subcommission on the Systematics of Igneous Rocks. *Cambridge University Press*, Cambridge, 1–236.

Leake B.E. 1978: Nomenclature of amphiboles. *American Mineralogist* 63, 1023–1052.

Leake B.E., Woolley A.R., Arps C.E.S., Birch W.D., Gilbert M.C., Grice J.D., Hawthorne F.C., Kato A., Kisch H.J., Krivovichev V.G., Linthout K., Laird J., Mandarino J.A., Maresch W.V., Nickel E.H., Rock N.M.S., Schumacher J.C., Smith D.C., Stephenson N.C.N., Ungaretti L., Whittaker E.J.W. & Youzhi G. 1997: Nomenclature of amphiboles: report on the Subcommittee on Amphiboles of the International Mineralogical Association, Commission on New Minerals and Mineral Names. *American Mineralogist* 82, 1019–1037.

Marks M., Halama R., Wenzel T. & Markl G. 2004: Trace element variations in clinopyroxene and amphibole from alkaline to peralkaline syenites and granites: implications for mineral–melt trace-element partitioning. *Chemical Geology* 211, 185–215. https://doi.org/10.1016/j.chemgeo.2004.06.032

Morimoto N., Fabries J., Ferguson A.K., Ginzburg I.V., Ross M., Seifert F.A., Zussman J., Aoki K. & Gottardi G. 1988: Nomenclature of pyroxenes. *American Mineralogist* 73, 1123–1133. https://doi.org/10.1007/BF01226262

Morogan V., Upton B.G.J. & Fitton J.G. 2000: The petrology of the Ditrău alkaline complex, Eastern Carpathians. *Mineralogy and Petrology* 69, 227–265. https://doi.org/10.1007/s007100070023

Naney M.T. 1983: Phase equilibria of rock-forming ferromagnesian silicates in granitic systems. *American Journal of Science* 283, 993–1033. https://doi.org/10.2475/ajs.283.10.993

Nesbitt H.W. & Young G.M. 1982: Early Proterozoic climates and plate motions inferred from major element chemistry of lutites. *Nature* 299, 715–717. https://doi.org/10.1038/299715a0

Nixon G.T. & Pearce T.H. 1987: Laser-interferometry study of oscillatory zoning in plagioclase: The record of magma mixing and phenocryst recycling in calc-alkaline magma chambers, Iztaccihuatl volcano, Mexico. *American Mineralogist* 72, 1144–1162.

Ódri Á., Harris C. & Le Roux P. 2020: The role of crustal contamination in the petrogenesis of nepheline syenite to granite magmas in the Ditrău Complex, Romania: evidence from O-, Nd-, Sr- and Pb-isotopes. Contributions to Mineralogy and Petrology 175, 100. https://doi.org/10.1007/s00410-020-01738-5

Pál-Molnár E. 2000: Hornblendites and diorites of the Ditrău Syenite Massif. *Department of Mineralogy, Geochemistry and Petrology, University of Szeged*, Szeged, 1–172.

Pál-Molnár E. 2021: Zárt és nyílt rendszerű magmás folyamatok a Ditrói Alkáli Masszívumban [Closed and open-system igneous processes in the Ditrău Alkaline Massif]. *Doctoral dissertation, Hungarian Academy of Sciences*, 1–136 (in Hungarian).

Pál-Molnár E., Batki A., Almási E.E., Kiss B., Upton B.G.J., Markl G., Odling N. & Harangi Sz. 2015a: Origin of mafic and ultramafic cumulates from the Ditrău Alkaline Massif, Romania. *Lithos* 239, 1–18. https://doi.org/10.1016/j.lithos.2015.09.022

Pál-Molnár E., Batki A., Ódri Á., Kiss B. & Almási E.E. 2015b: Geochemical implications of the magmatic origin of granitic rocks from the Ditrău Alkaline Massif (Eastern Carpathians, Romania). *Geologia Croatica* 68, 51–66. https://doi.org/10.4154/GC.2015.04

Pál-Molnár E., Kiri L., Lukács R., Dunkl I., Batki A., Szemerédi M., Almási E.E., Sogrik E. & Harangi Sz. 2021: Timing of magmatism of the Ditrău Alkaline Massif, Romania – A review based on new U–Pb and K/Ar data. *Central European Geology* 64, 18–37. https://doi.org/10.1556/24.2021.00001

Perugini D., Petrelli M. & Poli G. 2006: Diffusive fractionation of trace elements by chaotic mixing of magmas. *Earth and Planetary Science Letters* 243, 669–680. https://doi.org/10.1016/j.epsl.2006.01.026

Piwinskii A.J. 1968: Experimental studies of igneous rock series central Sierra Nevada batholith, California. *Journal of Geology* 76, 548–570.

Poli G., Tommasini S. & Halliday A.N. 1996: Trace elements and isotopic exchange during acid-basic magma interaction processes. *Transactions of the Royal Society of Edinburgh: Earth Sciences* 87, 225–232. https://doi.org/10.1130/0-8137-2315-9.225

Putirka K.D. 2005: Igneous thermometers and barometers based on plagioclase+liquid equilibria: Tests of some existing models and new calibration. *American Mineralogist* 90, 336–346. https://doi.org/10.2138/am.2005.1449

Săndulescu M. 1984: Geotectonica României [Geotectonics of Romania]. *Editura Technică* (in Romanian).

Săndulescu M., Kräutner H.G., Balintoni I., Russo-Săndulescu M. & Micu M. 1981: The structure of the East Carpathians (Moldavia – Maramures Area). Guide Exc. B1, XII Congress of the Carpathian Balkan Geological Association. *Institute of Geology and Geophysics*, Bucuresti.

Scaillet B., Holtz F. & Pichavant M. 2016: Experimental constraints on the formation of silicic magmas. *Elements* 12, 109–114. https://doi.org/10.2113/gselements.12.2.109

Schmidt M.W. 1992: Amphibole composition in tonalite as a function of pressure: an experimental calibration of the Al-in-hornblende barometer. *Contributions to Mineralogy and Petrology* 110, 304–310. https://doi.org/10.1007/BF00310745

Słaby E., Galbarczyk-Gasiorowska L. & Baszkiewicz A. 2002: Mantled alkali-feldspar megacrysts from the marginal part of the Karkonosze granitoid massif (SW Poland). *Acta Geologica Polonica* 52, 501–519.

Słaby E., Seltmann R., Kober B., Müller A., Galbarczyk-Gasiorowska L. & Jeffries T. 2007: LREE distribution patterns in zoned alkali feldspar megacrysts from the Karkonosze pluton, Bohemian Massif – implications for parental magma composition. *Mineralogical Magazine* 71, 193–217. https://doi.org/10.1180/minmag.2007.071.2.155

Słaby E., Śmigielski M., Śmigielski T., Domonik A., Simon K. & Kronz A. 2011: Chaotic three-dimensional distribution of Ba, Rb, and Sr in feldspar megacrysts grown in an open magmatic system. *Contributions to Mineralogy and Petrology* 162, 909–927. https://doi.org/10.1007/s00410-011-0631-6

Smith V.C., Blundy J.D. & Arce J.L. 2009: A temporal record of magma accumulation and evolution beneath Nevado de Toluca, Mexico, preserved in plagioclase phenocrysts. *Journal of Petrology* 50, 405–426. https://doi.org/10.1093/petrology/egp005

Sparks R.S.J. & Marshall L.A. 1986: Thermal and mechanical constraints on mixing between mafic and silicic magmas. *Journal of Volcanology and Geothermal Research* 29, 99–124. https://doi.org/10.1016/0377-0273(86)90041-7

Streckeisen A. & Hunziker I.C. 1974: On the origin of the Nephelinesyenite Massif of Ditró (Transylvania, Romania). *Schweizerische Mineralogische und Petrographische Mitteilungen* 54, 59–77.

Streckeisen A. & Le Maitre R.W. 1979: A chemical approximation to the modal QAPF classification of the igneous rocks. *Neues Jahrbuch für Mineralogie, Abhandlungen* 136, 169–206.

Sun S. & McDonough W.F. 1989: Chemical and isotopic systematics of oceanic basalts: implications for mantle composition and processes. *Geological Society, London, Special Publications* 42, 313–345. https://doi.org/10.1144/GSL.SP.1989.042.01.19

Tang G.-J., Wang Q., Wyman D.A., Dan W., Ma L., Zhang H.-X. & Zhao Z.H. 2020: Petrogenesis of the Ulungur Intrusive Complex, NW China, and implications for crustal generation and reworking in accretionary orogens. *Journal of Petrology* 61. https://doi.org/10.1093/petrology/egaa018

Ubide T., Galé C., Arranz E., Lago M. & Larrea P. 2014a: Clinopyroxene and amphibole crystal populations in a lamprophyre sill from the Catalonian Coastal Ranges (NE Spain): a record of magma history and a window to mineral-melt partitioning. *Lithos* 184–187, 225–242. https://doi.org/10.1016/j.lithos.2013.10.029

Ubide T., Galé C., Larrea P., Arranz E., Lago M. & Tierz P. 2014b: The relevance of crystal transfer to magma mixing: a case study in composite dykes from the Central Pyrenees. *Journal of Petrology* 55, 1535–1559. https://doi.org/10.1093/petrology/egu033

van Achterbergh E., Ryan C.G., Jackson S.E. & Griffin W.L. 2001: Data reduction software for LA-ICP-MS. In: Sylvester P.J. (Ed.): Laser Ablation-ICP-Mass spectrometry in the earth sciences: principles and applications. Short Course Series, 29. *Mineralogical Association of Canada*, St. John's, Newfoundland, 239–243.

Vance J.A. 1969: On synneusis. *Contributions to Mineralogy and Petrology* 24, 7–29. https://doi.org/10.1007/BF00398750

Vernon R.H. 1984: Microgranitoid enclaves – globules of hybrid magma quenched in a plutonic environment. *Nature* 304, 438–439. https://doi.org/10.1038/309438a0

Vernon R.H. 1990: Crystallization and hybridism in microgranitoid enclave magmas: Microstructural evidence. *Journal of Geophysical Research* 95, 17849–17859. https://doi.org/10.1029/JB095iB11p17849

Vernon R.H. & Collins W.J. 2011: Structural criteria for identifying granitic cumulates. *Journal of Geology* 119, 127–142. https://doi.org/10.1086/658198

Whitney D.L. & Evans B.W. 2010: Abbreviations for names of rock-forming minerals. *American Mineralogist* 95, 185–187. https://doi.org/10.2138/am.2010.3371

Wiebe R.A. 1968: Plagioclase stratigraphy; a record of magmatic conditions and events in a granite stock. *American Journal of Science* 266, 690–703. https://doi.org/10.2475/ajs.266.8.690

Wiebe R.A., Smith D., Sturm M., King E.M. & Seckler M.S. 1997: Enclaves in the Cadillac Mountain Granite (Coastal Maine): Samples of hybrid magma from the base of the chamber. *Journal of Petrology* 38, 393–423. https://doi.org/10.1093/petroj/38.3.393

Electronic supplementary material is available online:

Supplementary Figures S1–S3 at http://geologicacarpathica.com/data/files/supplements/GC-74-4-Kiri-FigsS1-S3.docx

Supplementary Tables S1–S9 at http://geologicacarpathica.com/data/files/supplements/GC-74-4-Kiri-TablesS1-S9.xlsx

Supplement

Fig. S1. Compositional variation of the analysed clinopyroxenes in terms of the En–Fs–Wo end-members (Morimoto et al. 1988). The clot-forming and orbicular inclusion-derived clinopyroxene data are marked with symbols with a black rim.
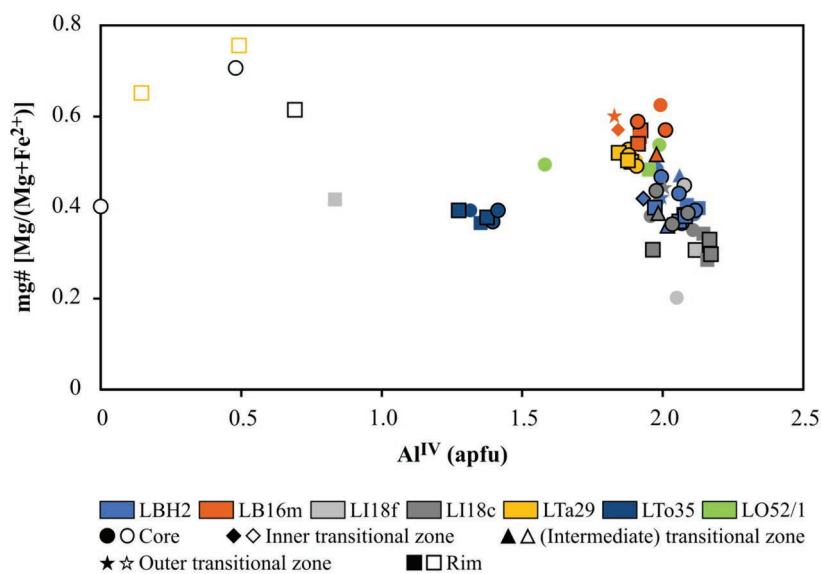
Fig. S2. Compositional variation of the analysed amphiboles in terms of their mg# and Al^{IV} concentration. Actinolite data are marked by empty symbols. The compositions of the clot-forming crystals are identified by symbols with a black rim.
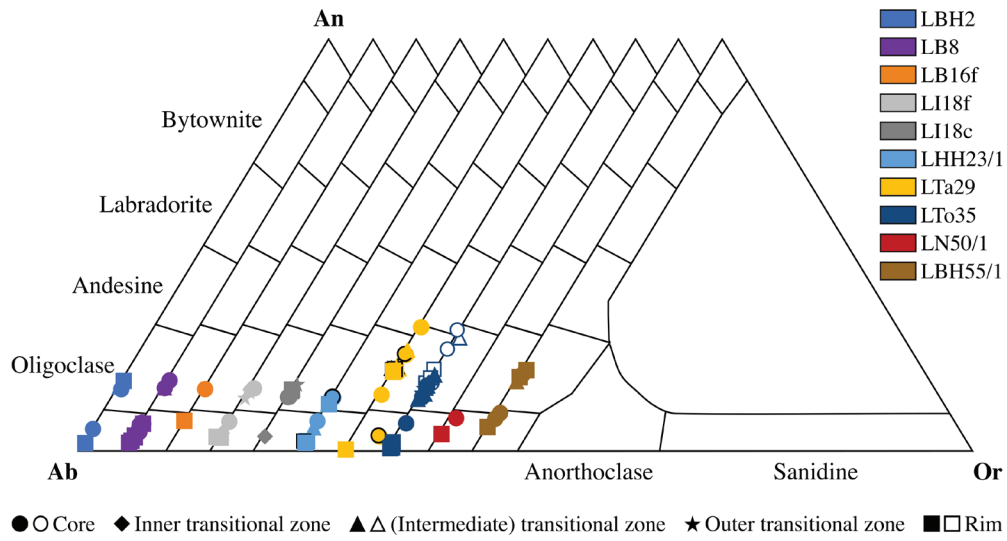
Fig. S3. Compositional variation of the analysed plagioclase crystals in terms of the Ab–An–Or end-members. Data of plagioclase in synneusis are marked by empty symbols. The composition of the clot-forming crystals is identified by symbols with a black rim.